VIBRATION REDUCTION BY SHAPING THE TERRAIN TOPOGRAPHY

PER JØRSTAD

VIBRATION REDUCTION BY SHAPING THE TERRAIN TOPOGRAPHY

Master's Dissertation by

PER JØRSTAD

Supervisor:

Peter Persson, *M.Sc.,*
Div. of Structural Mechanics, LTH, Lund

Examiner:

Kent Persson, *PhD,*
Dept. of Construction Sciences, LTH, Lund

Preface

Having started in June 2011, this Master's Dissertation, carried out at the Division of Structural Mechanics at Lund University Faculty of Engineering, has come to a conclusion in June 2012 – which also marks the end of my Master's degree in Civil and Structural Engineering.

For coming up with the inspiring idea and for support and decisive guidance during this project, I would like to thank my examiner, Ph.D. Kent Persson, at the Division of Structural Mechanics. It has been an honour to get to work with this extraordinary subject, which is of the kind that engages people in general and will certainly follow me in my future professional career. The same gratitude is also dedicated to M.Sc. and Ph.D. student Peter Persson at Division of Structural Mechanics, my supervisor, for guidance, discussions and dedication throughout this thesis.

Furthermore, the staff at Altair Engineering in Lund deserves a significant amount of honour for making this work happen. This project would not have been the same without the software and efficient support provided – thank you especially Magnus Hermodsson and Dag Thuvesen.

For having prepared me for this Master's Dissertation during the past six years, I would, in addition to the Lund University Faculty of Engineering also like to thank the staff at Norwegian University of Science and Technology in Trondheim, Norway, as well as Université Joseph Fourier Grenoble 1 in Grenoble, France. I have ended up getting my education at what in my perception are three very good universities.

Finally, I would like to thank those close to me – my parents, Anna and Jan, for always being supportive, and my brother, civil and structural engineering student Anders, for continuous valuable input to my work. The very last expression of gratitude is directed towards my girlfriend, Linnéa, for her patience and help through many late nights working on this project.

Lund, June 2012

Per Jørstad

Abstract

MAX-lab is a synchrotron radiation laboratory run in cooperation between Lund University and the Swedish Research Council. It currently consists of three storage rings, however, construction has begun of the fourth. MAX IV will be located outside of the Lund University Faculty of Engineering campus, in the northeastern part of Lund. Induced by the development in material technology at the nanometer level, the state-of-the art facility will become a landmark with its large storage ring that has a circumference of approximately 500 m. The instruments operating at MAX IV are extremely sensitive to vibrations, which has led to the establishment of a strict upper level limit. A number of actions has been taken on site, including the implementation of a landscape of hills and valleys surrounding the facility, that should distort and damp out external vibration induced waves traveling in the ground. One of the most concerning sources of vibrations from the surroundings is the highway, E22, passing 100 m to the west of the facility.

As the shaped landscape of hills and valleys is not currently extended to cover the area between MAX IV and the highway, this Master's Dissertation has investigated the possible gain in vibration reduction by making this extension. Finite element models in two and three dimensions have been established, onto which a variety of shapes has been applied. Harmonic unit point loading has been used in the steady-state analysis, spanning from 5–20 Hz (as higher frequency waves are damped out quickly). With the low magnitude loading, visco-elastic isotropic behaviour has been applied to the clay and bedrock, modeled with properties derived by commercial contractors and consultants on the MAX IV site. All shapes applied are derived from a set of arcs with constant curvature, and a practical limit in slope angle of 30°. This has led to a maximum difference in altitude of approximately 20 m. On the far side of the shape zone, 100 m from the loading point, a main evaluation point has been investigated, supported by a number of additional evaluation points. The main focus of this project has been vertical displacements.

In the 2D analyses some clear tendencies could be seen. The application of fewer hills and valleys of large magnitude provided the best results compared to a flat terrain, with reductions in RMS vertical displacements of more than 20 %. Reductions were seen for all of the applications with altering hills and valleys as long as the net change in material was positive or zero. Reductions in vertical displacements were also seen for all applications when only hills were applied. A negative effect was seen when applying only valleys or having an altering pattern with more valleys than hills for smaller magnitude level differences. Another tendency seen for the altering applications was that a hill seems to perform better when it is preceded by a valley, i.e. a smooth transition rather than an abrupt.

In the 3D analyses that corresponded to the 2D analyses, the same tendencies could be seen, with reductions of the same magnitude. From visualizations, it could also be seen that a continuous hill actually captures the waves and directs them in the

longitudinal direction of the hill. A better caption was obtained when rotating the hills horizontally to not run transversally across the model, but in an angle. For this case, however, the risk of transmitting an intensified wave front in the direction of the evaluation points emerges. A checkered pattern of elevations and depressions showed the same tendencies – the waves tended to follow paths of elevations. This explains why some configurations of checkered patterns provided reductions in vertical displacements whereas others increased the displacements at the evaluation points.

Ultimately, it became clear that some of the tested shape configurations are safe choices, whereas others seem to possibly reduce vertical displacements to a larger extent locally but with the risk of intensifying them elsewhere.

Contents

1 Introduction

1.1 Background

"Seeing the invisible" is the title of Professor Mikael Eriksson's (Head of the Accelerator Physics Department at Lund University Faculty of Engineering and Machine Director at MAX-lab) popular science lecture about MAX IV. More precisely, MAX-lab, with MAX referring to Microtron Accelerator for X-rays, is a national facility for "research with synchrotron radiation and energetic electrons", operated jointly by Lund University and the Swedish Research Council [1]. On the basis of the electron accelerator, LUSY (Lund University Synchrotron), constructed in 1962, MAX-lab got governmental fundings in 1982 and moved in to their current laboratory on the Faculty of Engineering at Lund University in 1983. The first storage ring, MAX I, was officially operative in 1987. Today the facility consists of MAX I, II and III, three storage rings which are all located in the same laboratory, using the same electron pre-accelerator, MAX-injector.

The principle of synchrotron radiation facilities begins with electrons being accelerated to near light speed in an electron pre-accelerator (like the MAX-injector). The electrons then enter a storage ring where a magnetic field caused by strong magnets in the ring controls the electrons' closed circular path. This causes the electrons to emit an extremely high-energy electromagnetic radiation, named synchrotron light. The synchrotron light is focused into a number of tangentially installed beam lines on the ring, allowing researchers to "see the invisible" in research stations at the end of the beam lines – i.e. using the synchrotron light to study structures at the nanometer level. For the more unfamiliar, the parallel may be drawn to conventional x-ray instruments that you find in hospitals, and indeed, the synchrotron radiation is partly in the x-ray spectrum, but with an intensity and energy level that far exceeds that of the former.

As research is progressing, there is now need for an upgrade of the synchrotron radiation facility. Construction has therefore already begun (during 2010) of the MAX IV, the new state-of-the-art national synchrotron radiation facility. It will consist of a an electron pre-accelerator, i.e. an electron gun, supplying a linac (linear accelerator) with electrons, that are accelerated into two new storage rings,
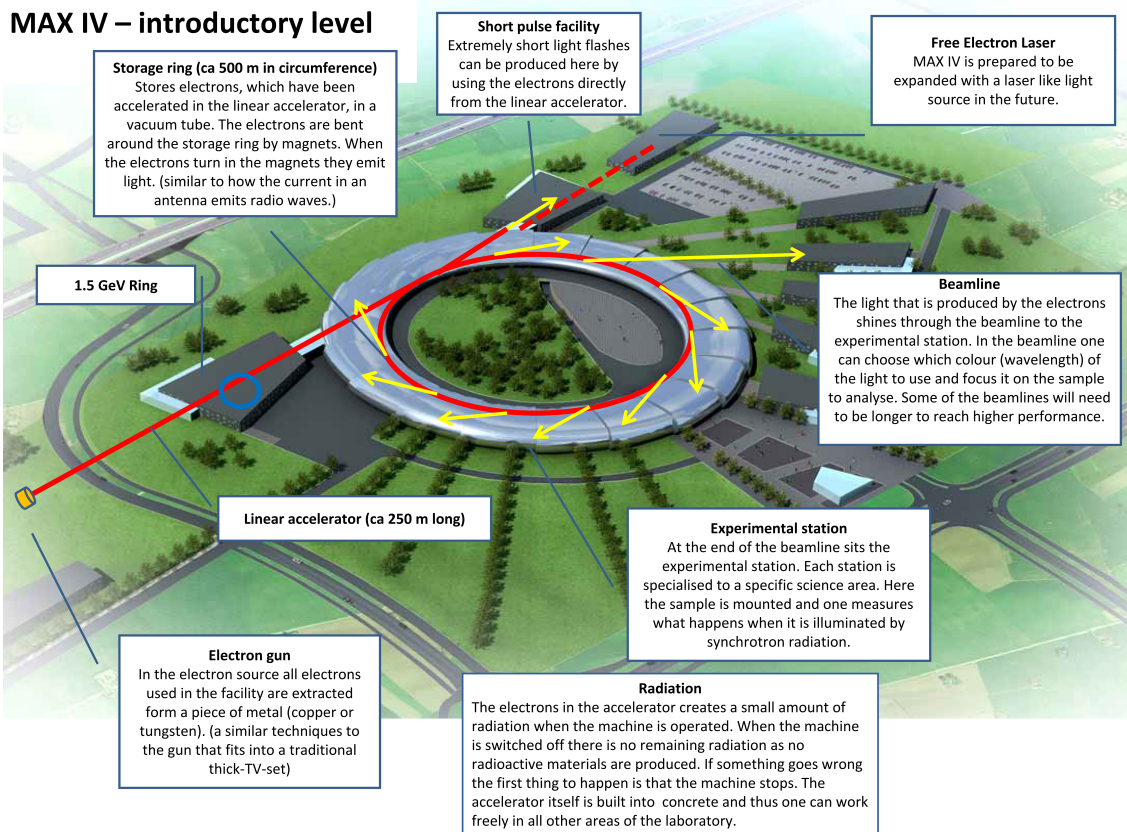
MAX IV – introductory level

Storage ring (ca 500 m in circumference)
Stores electrons, which have been accelerated in the linear accelerator, in a vacuum tube. The electrons are bent around the storage ring by magnets. When the electrons turn in the magnets they emit light. (similar to how the current in an antenna emits radio waves.)

Short pulse facility
Extremely short light flashes can be produced here by using the electrons directly from the linear accelerator.

Free Electron Laser
MAX IV is prepared to be expanded with a laser like light source in the future.

1.5 GeV Ring

Beamline
The light that is produced by the electrons shines through the beamline to the experimental station. In the beamline one can choose which colour (wavelength) of the light to use and focus it on the sample to analyse. Some of the beamlines will need to be longer to reach higher performance.

Linear accelerator (ca 250 m long)

Experimental station
At the end of the beamline sits the experimental station. Each station is specialised to a specific science area. Here the sample is mounted and one measures what happens when it is illuminated by synchrotron radiation.

Electron gun
In the electron source all electrons used in the facility are extracted form a piece of metal (copper or tungsten). (a similar techniques to the gun that fits into a traditional thick-TV-set)

Radiation
The electrons in the accelerator creates a small amount of radiation when the machine is operated. When the machine is switched off there is no remaining radiation as no radioactive materials are produced. If something goes wrong the first thing to happen is that the machine stops. The accelerator itself is built into concrete and thus one can work freely in all other areas of the laboratory.

Figure 1.1: The principle of a synchrotron radiation facility: Early sketches of MAX IV with explanation [1].

of which the largest one has a circumference of 528 meters and an energy level of 3.0 GeV. A planned number of 20 research stations will be constructed throughout the ring. The linac also supplies electrons to a separate short pulse facility (SPF) that may be used to investigate very short instant nano-scaled structural phenomena. Furthermore, MAX IV is prepared for a possible expansion with a free electron laser (FEL), which allows for even more extreme sample conditions.

MAX IV will serve a large number of research areas, e.g. material technology, medicine, biology, archeology and paleontology. And with the obvious spatial demands of the facility, it will be built outside of the current Lund University Campus, on past farming land in the northeastern part of Lund.

Having instruments operating at the nanometer level imply extreme demands not only on the instruments themselves, but also on the stability of their foundations. MAX IV will be equipped with an active calibration system that can handle incoming vibrations from the surroundings between 0–5 Hz up to 260 nm. For frequencies higher than 5 Hz, however, there is a limit of vertical displacements of 26 nm RMS (root mean square) during one second. For frequencies over 100 Hz, the response is so low it may be neglected. In order to handle the strict requirements, a number

of actions will be taken. The soil underneath the ring will be stabilized (stiffened) by mixing cement into the underlaying layer of clay till. Furthermore, initial calculations imply that shaping the surrounding ground surface into a landscape of hills and valleys will reduce the incoming surface waves. This is also an aesthetically desirable solution, as the facility should serve the role as a landmark and a symbol of Lund as a technological capital. The solution has been accepted and the landscape architecture is carried out in cooperation between architect bureaus Fojab and Snøhetta.

On the east side of MAX IV there is a smaller road with vehicles passing by, causing vibrations. More concerning in terms of vehicle induced vibrations, however, is the four-lane highway, E22, passing 100 m to the west of the site (see Figure 1.2).

Figure 1.2: Architectural solution at MAX IV. View from the north, image by Fojab [1].

1.2   Objective and Method

The objective of this Master's Dissertation was to investigate the effects of applying different shapes to an initially flat terrain through which traffic vibration induced waves propagate. The work has focused on vertical displacements. It has been a general study on which the conditions at MAX IV were applied. This way, it may also, in the case of well-documented vibration reducing properties, serve as an incentive to extend the landscape of hills and valleys which is already planned at MAX IV into incorporating the area between the facility and the closely passing highway.

The finite element method has been employed to model the area between the highway and MAX IV, and vibrations induced by passing vehicles were applied in the form of harmonic point loading. Efficient finite element models were developed, onto which a limited variation of shapes were applied. Analyses were carried out in both two and three dimensions.

1.3   Disposition

The following chapters are included in this Master's Dissertation report:

- Chapter 2 describes the prerequisites for this project, i.e. the properties and composition of the soil and the present loads on site.

- Chapter 3 is an introduction to the applied theory, such as dynamics, wave propagation and the finite element method.

- Chapter 4 is a presentation of the finite element models and analysis setup in two and three dimensions.

- Chapter 5 contains the results in detail.

- Chapter 6 is dedicated to conclusions, discussion and suggestions to possible further work.

2 Prerequisites

2.1 Materials

2.1.1 Composition of the Soil

The city of Lund is located on a continous slope that has its lower point in one end and its highest point in the other end of the city, the latter in the northeastern part where MAX IV is located. The geological explanation to this is the fact Lund lies on the front end of a long and narrow hill (Romeleåsen) caused by one of several faults between the Eastern European tectonic plate and the Baltic Shield. Further east on the fault, parent rock (gneiss) may be encountered on the surface. On the MAX IV site, however, the bedrock starting at 12-17 m depth consists of shale, limestone and sandstone [2].

The layers covering the bedrock are identified as Low Baltic clay till and Northeast clay till (starting from the surface) [1]. These layers were created as a result of the last ice age. They are glacial sediments from the moraines of the retreating ice. The fact that they are fine graded (clay) derives from the ice's degradation of the already mentioned underlying bedrock. Ice covered Northern Europe from around 100,000 years ago, until the climate changed about 20,000 years ago, causing the ice to retreat slowly. The city of Lund was ice free approximately 15,000 years ago, with the ice at this time retreating at a rate of 50 m/year.

Clay is a cohesive soil, meaning that the shear capacity is obtained mainly from cohesion between the particles themselves. It has a low permeability but does often contain a lot of water providing a Poisson's ratio, ν, close to 0.5. Maximum slope angle on the surface is $30°$. With the cohesiveness of the clay, it is obvious that it would initially be possible to create steeper slopes, which can be seen in Figure 2.1, but in a long term perspective, the $30°$ limit is reasonable [8].

Preconsolidated soil (which is the case on the MAX IV site due to the loading of the ice in the past) may be regarded as elastic at loading inferior to the preconsolidation pressure. The loading investigated in this thesis will be significantly lower than the preconsolidation pressure [10]. (In this matter, reference may also be made to section 3.2.2.)

Figure 2.1: Digging of the Linac tunnel. Image courtesy of Annika Nyberg [1].

2.1.2   Soil Properties

The soil properties vary throughout the site of MAX IV. The chosen soil profile in this thesis is situated in the area where the linac is attached to the ring. The two layers of clay have the same properties at this location.

Table 2.1: Material properties [9].

	Clay	Bedrock
Depth [m]	14.0	-
Density [kg/m^3]	2125	2600
Young's modulus [MPa]	476	8809
Poisson's ratio [-]	0.48	0.40
Loss factor [-]	0.14	0.04
P-wave velocity [m/s]	1402	2694
S-wave velocity [m/s]	275	1100

2.2 Loads

In terms of vibrations, Norwegian Geotechnical Institute in cooperation with representatives from contractor PEAB have done measurements on site using triaxial accelerometers and vertical geophones placed in a number of different locations throughout the location. These measurements allow them to present values in Table 2.2 (in one third octave bandwiths) of the vertical displacements per frequency at a point approximately 100 meters from the highway (where the MAX IV main building begins) [9]. These values should be interpreted as displacements due to a combination of the loading per frequency from traffic and the possible amplification of these at certain frequencies because of the eigenfrequencies and geometry of the soil profile.

Table 2.2: Vertical displacement per frequency at MAX IV 100 m from the highway [9].

Frequency [Hz]	Vertical displacement [nm]
5	28.8
6.3	46.4
8	38.0
10	37.0
12.5	15.0
16	7.30
20	1.50

3 Theory

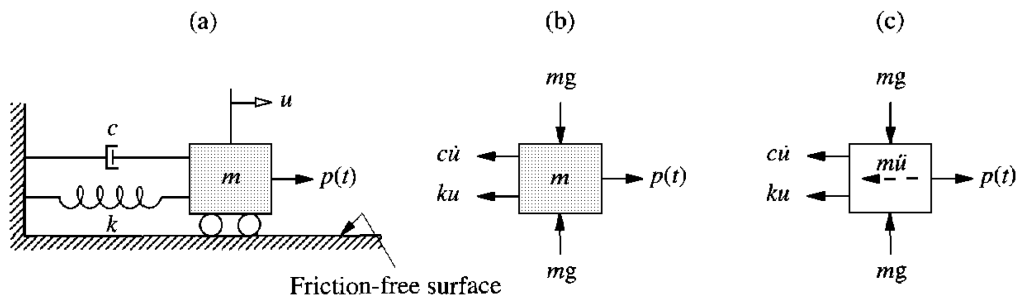## 3.1 Dynamics Theory

3.1.1 General

Figure 3.1: SDOF-model [3].

The simplest way of describing dynamic motion is by looking at an SDOF model (single degree of freedom). An example of such a model is presented in Figure 3.1, where a mass, m, is excited in the only degree of freedom, the displacement u, by a time-dependent force, $p(t)$, and restrained by a spring with stiffness k and a damper with constant c that provides a damping force which is proportional to the velocity of the mass.

Recalling Hooke's law for springs gives us the reaction force from the spring

$$f_S = ku \tag{3.1}$$

For the damper, we get

$$f_D = c\dot{u} \tag{3.2}$$

where the overdot denotes differentiation with respect to time. The resultant force is then

$$F = p(t) - (f_S + f_D) = p(t) - ku - c\dot{u} \tag{3.3}$$

Newton's second law implies

$$F = ma = m\ddot{u} \tag{3.4}$$

Sorting and rewriting the equations give us the equation of motion for an SDOF system

$$m\ddot{u} + c\dot{u} + ku = p(t) \tag{3.5}$$

In order to describe the motion of a an MDOF system (multiple degrees of freedom), such as a finite element model, the equation of motion is stated as a matrix formulation

$$\mathbf{M\ddot{u}} + \mathbf{C\dot{u}} + \mathbf{Ku} = \mathbf{P}(t) \tag{3.6}$$

where $\mathbf{M}$, $\mathbf{C}$ and $\mathbf{K}$ are the mass, damping and stiffness matrix, respectively. $\mathbf{P}(t)$ is the load vector and $\mathbf{u}$ is the displacement vector.

3.1.2   Steady-State Frequency Response

In dynamic analysis of a damped system with forced harmonic vibration one distinguishes between the transient and the steady-state response. The transient response is visible during the beginning of the loading but is damped out, leaving the steady-state response which has the same frequency as the harmonic loading. This is exemplified in Figure 3.2.

The subsequent derivation of the relation between the force and the steady-state response is based on [4]. With harmonic loading, e.g.

$$\mathbf{P}(t) = \mathbf{P_0}\sin(\omega t) \tag{3.7}$$

the load and displacement vectors may be written in complex form

$$\mathbf{P}(t) = \mathbf{\hat{P}}\mathrm{e}^{\mathrm{i}\omega t} \tag{3.8}$$

$$\mathbf{u}(t) = \mathbf{\hat{u}}\mathrm{e}^{\mathrm{i}\omega t} \tag{3.9}$$
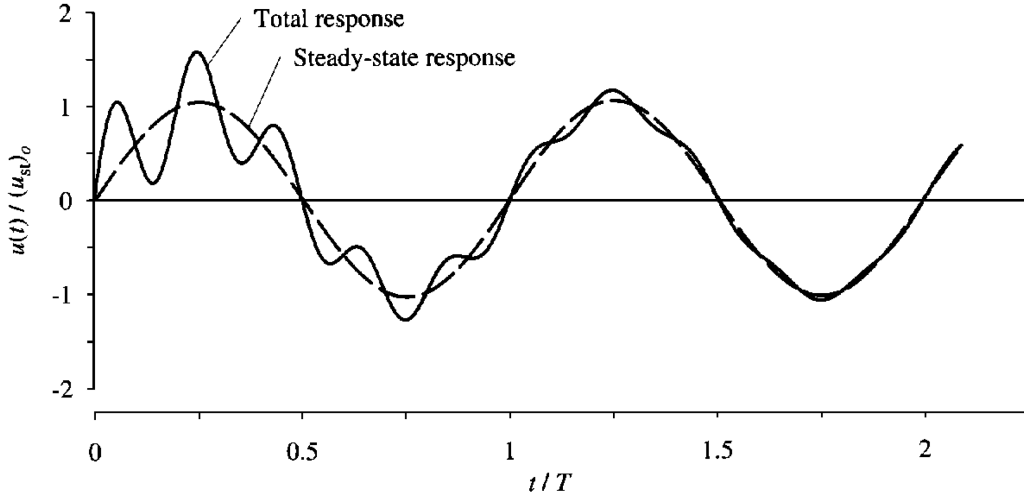
Figure 3.2: Total and steady state response of a damped system subjected to harmonic loading [3].

where $\hat{\mathbf{P}}$ and $\hat{\mathbf{u}}$ are the complex load and displacement amplitudes respectively, i is the complex number $\sqrt{-1}$, ω is the angular frequency and t denotes the time. Inserting these formulations into (3.6) allows us to eliminate the time dependancy, providing us with

$$\mathbf{D}(\omega)\hat{\mathbf{u}} = \hat{\mathbf{P}} \tag{3.10}$$

where $\mathbf{D}(\omega)$ is the dynamic stiffness matrix that, depending on the frequency, ω, provides the steady state response:

$$\mathbf{D}(\omega) = -\omega^2\mathbf{M} + \mathrm{i}\omega\mathbf{C} + \mathbf{K} \tag{3.11}$$

3.1.3 Loss Factor

Damping in a dynamic mechanism may be introduced in different ways, e.g. in terms of the loss factor, ξ, which may be written as

$$\xi = \frac{1}{2\pi}\frac{E_D}{E_{S_0}} \tag{3.12}$$

where

$$E_D = \pi c\omega u_0^2 \tag{3.13}$$

is the energy dissipated due to viscous damping in one cycle of motion in an SDOF system. All parameters are introduced in preceding sections except for u_o, which should be interpreted as the amplitude of the motion. This equation also shows the relation with the damping constant, c. Furthermore,

$$E_{S_0} = ku_0^2/2 \tag{3.14}$$

is the maximum strain energy in the spring. The loss factor is also denoted the specific damping factor [3]. The fraction between the energy loss and the maximum strain energy is shown in Figure 3.3.
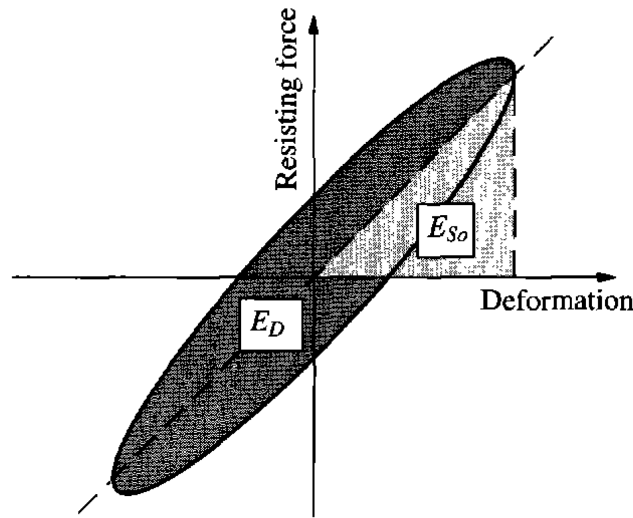
Figure 3.3: Energy loss, E_D, and maximum strain energy, E_{S_0}, in one cycle of harmonic vibration [3].

3.1.4   RMS-Value

RMS is short for "Root Mean Square" and is a convenient interpretation of the mean value of dynamic responses, as it provides the amplitude regardless of the sign (which for dynamic responses obviously may vary). The root mean square of a set n of values, when considering displacements, u, is given as

$$u_{RMS} = \sqrt{\frac{1}{n}\sum_{i=1}^{n} u_i^2} \tag{3.15}$$

For a continuous frequency response function, FRF, the value is given as

$$u_{RMS} = \sqrt{\frac{1}{\Delta f} \int_{f_0}^{f_0 + \Delta f} u^2(t) \mathrm{d}f} \tag{3.16}$$

3.2 Wave Propagation Theory

For further reading and for reference on this subject, see [7].

3.2.1 Wave Propagation in a Linear Elastic Material

In a linear elastic material there are mainly three different types of waves that occur due to dynamic loading. Those are P-, S- and Rayleigh-waves. P-waves travel throughout the volume of a given material and have the highest phase velocity. Thus, they are known as primary waves. But there is a duality of the letter P, i.e. the P-wave motion works as a change in pressure. The duality can also be applied to the S-waves as they are secondary waves with a particle motion in equivoluminal shear. As the P-wave, they travel in volume, although at a phase velocity that is about half of that of the former. The particle motion in P- and S-waves can be seen in Figure 3.4. Rayleigh-waves travel only on the surface of the ground and is a mix of pressure and shear. They have the slowest phase velocity of the three at approximately 90 % of that of the S-wave.
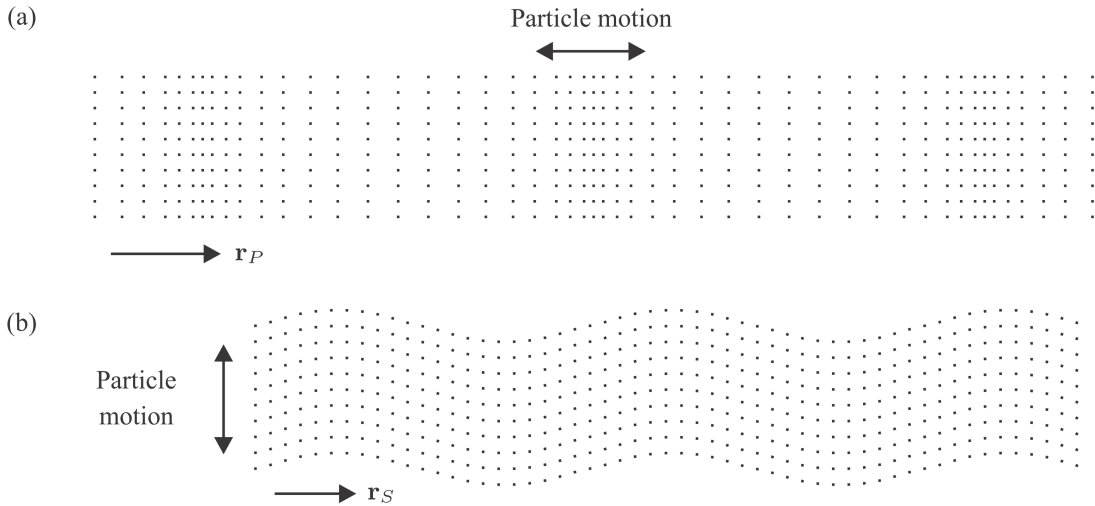

Figure 3.4: Particle motion in plane P-waves (a) and plane S-waves (b). The unit vectors $\mathbf{r}_P$ and $\mathbf{r}_S$ denote the direction of the wave propagation [7].

3.2.2 Soil as a Linear Elastic Material

In many fields of civil engineering, soil is not considered to be a linear elastic material. Even in soil dynamics, e.g. when analyzing earthquakes, stresses may be of such magnitude that plasticity cannot be neglected. However, for human made ground borne vibrations, stresses are usually at such a level, an assumption of linear elasticity suffices. As for damping, it generally does play an important role in terms of the dynamic response and is therefore usually applied to the linear elastic material, which evidently makes it a visco-elastic material model. Since P-waves and S-waves spread in the volume of the soil, they are damped out much faster, i.e. closer to the source of vibration, than the Rayleigh-waves, which are only affected by damping close to the surface.

3.2.3 Soil as a Homogeneous Material

Soil is in reality not a homogeneous material (refer to e.g. the granularity of a soil). However, for wave propagation, local variations does not have a large influence. Lars Andersen draws the following picture: In most soils, Rayleigh-waves have a phase speed of more than 100 m/s, which means that they have a wave length of 1 m at a frequency of 100 Hz. The local variations in a soil is usually considerably inferior to that and therefore do not play a significant role. Thus, a homogeneous material model is plausible.

To deal with more global phenomena such as settlements, cementation and consolidation of a soil material due to the depth of a certain layer, dividing the given layer into several layers with different elastic properties may be necessary.

3.2.4 P- and S-wave Speeds for Linear Elastic Homogeneous Isotropic Materials

In deriving the expressions for the P- and S-wave phase speeds, two constants are utilised, denoted the Lamé constants, given as

$$\lambda = \frac{\nu E}{(1+\nu)(1-\nu)}; \qquad \mu = \frac{E}{2(1+\nu)} \qquad (3.17)$$

where E is the Young's modulus and ν is the Poisson's ratio. Furthermore, μ is recognisable as the shear modulus, usually denoted G. Derivation according to [7] allows for the following ecpressions of the phase speed for P- and S-waves respectively for linear elastic homogeneous isotropic materials:

$$c_P = \sqrt{\frac{\lambda+2\nu}{\rho}}; \qquad c_S = \sqrt{\frac{\mu}{\rho}} \qquad (3.18)$$

respectively, where ρ is the density of the material.

3.3 The Finite Element Method

3.3.1 General

The finite element method is a numerical approximation method that is used to solve phenomena in a large number of engineering diciplines, as well as physics and mathematics, involving differential equations. On the basis of some basic principles presented by mathematicians in the early 1940's, the finite element method, as we know it today, was developed by mechanical engineers in the 50's [5]. With the addition of a more extensive mathematical foundation in the early 70's, the method has developed parallelly to the development of digital computational power into becoming one of the most important tools within its area [6].

The method is based on dividing a given region in one or several dimensions, over which some physical phenomenon governed by differential equations needs to be investigated, into a number of finite elements. Instead of approximating the possibly highly variable behaviour of the whole region, simpler (e.g. linear or quadratic) behaviour may be applied to each element. Rules are given for the patching together of the elements into what is denoted the element mesh, so that they work together in a proper way, providing an approximation for the whole region. A finer element mesh generally provides a more accurate approximation, in addition to requiring more computational power. Solution demands known boundary conditions for all borders [11].

3.3.2 FE formulation of Three-Dimensional Elasticity

The following derivation of the finite element method for three-dimensional elasticity is based on [11]. The differential equation of static equilibrium is given as

$$\tilde{\nabla}^{\mathrm{T}}\boldsymbol{\sigma} + \mathbf{b} = \mathbf{0} \tag{3.19}$$

where $\tilde{\nabla}$ is a matrix differential operator, σ is a vector composed of all the stress components and $\mathbf{b}$ is the body force vector containing the body forces per unit volume. Thus

$$
\tilde{\nabla}^{\mathrm{T}} = \begin{bmatrix} \frac{\partial}{\partial x} & 0 & 0 & \frac{\partial}{\partial y} & \frac{\partial}{\partial z} & 0 \\ 0 & \frac{\partial}{\partial y} & 0 & \frac{\partial}{\partial x} & 0 & \frac{\partial}{\partial z} \\ 0 & 0 & \frac{\partial}{\partial z} & 0 & \frac{\partial}{\partial x} & \frac{\partial}{\partial y} \end{bmatrix} \qquad \boldsymbol{\sigma} = \begin{bmatrix} \sigma_{xx} \\ \sigma_{yy} \\ \sigma_{xy} \\ \sigma_{xz} \\ \sigma_{yz} \end{bmatrix} \qquad \mathbf{b} = \begin{bmatrix} b_x \\ b_y \\ b_z \end{bmatrix} \qquad (3.20)
$$

Matrix multiplication of (3.19) then gives

$$
\begin{aligned}
\frac{\partial \sigma_{xx}}{\partial x} + \frac{\partial \sigma_{xy}}{\partial y} + \frac{\partial \sigma_{xz}}{\partial z} + b_x &= 0 \\
\frac{\partial \sigma_{xy}}{\partial x} + \frac{\partial \sigma_{yy}}{\partial y} + \frac{\partial \sigma_{yz}}{\partial z} + b_y &= 0 \\
\frac{\partial \sigma_{xz}}{\partial x} + \frac{\partial \sigma_{yz}}{\partial y} + \frac{\partial \sigma_{zz}}{\partial z} + b_z &= 0
\end{aligned} \qquad (3.21)
$$

Whereas the body force vector, **b**, acts on the body per unit volume, the traction vector, given as

$$
\mathbf{t} = \begin{bmatrix} t_x \\ t_y \\ t_z \end{bmatrix} \qquad (3.22)
$$

acts on the surface of the body, as a force per unit area. Being present on the surface, the traction vector has to fulfill the boundary condition

$$
\begin{aligned}
t_x &= \sigma_{xx} n_x + \sigma_{xy} n_y + \sigma_{xz} n_z \\
t_y &= \sigma_{xy} n_x + \sigma_{yy} n_y + \sigma_{yz} n_z \\
t_z &= \sigma_{xz} n_x + \sigma_{yz} n_y + \sigma_{zz} n_z
\end{aligned} \qquad (3.23)
$$

where the vector components n_x, n_y, and n_z make up the unit vector, **n**, normal to the boundary. In order to derive the weak form of the FE formulation, the arbitrary vector, **v** is introduced, given as

$$
\mathbf{v} = \begin{bmatrix} v_x \\ v_y \\ v_z \end{bmatrix} \qquad (3.24)
$$

Multiplication of the equations in (3.21) in the stated order by v_x, v_y, and v_z respectively, integrating the expressions over the volume, V, followed by an integration by parts using the Green-Gauss theorem (where the components of the traction vector emerges) and finally adding together the three expressions, provides the weak form of the differential equations of equilibrium

$$\int_V (\tilde{\nabla}\mathbf{v})^\mathrm{T}\boldsymbol{\sigma}\mathrm{d}V = \int_S \mathbf{v}^\mathrm{T}\mathbf{t}\mathrm{d}S + \int_V \mathbf{v}^\mathrm{T}\mathbf{b}\mathrm{d}V \tag{3.25}$$

also denoted the virtual work equation (recalling that $\mathbf{v}$ is arbitrary). In order to utilize this in the final FE formulation, the displacements vector, $\mathbf{u}$, is approximated by

$$\mathbf{u} = \mathbf{Na} \tag{3.26}$$

with $\mathbf{N}$ containing the global shape functions and $\mathbf{a}$ the displacements. Using the Galerkin method implies

$$\mathbf{v} = \mathbf{Nc} \tag{3.27}$$

where $\mathbf{c}$ is arbitrary (as $\mathbf{v}$ is arbitrary). This allows us to continue to

$$\tilde{\nabla}\mathbf{v} = \mathbf{Bc} \quad \text{where} \quad \mathbf{B} = \tilde{\nabla}\mathbf{N} \tag{3.28}$$

Inserting (3.27) and (3.28) into the weak form, (3.25), allows us to extract and eliminate $\mathbf{c}$ (as it is independent of the coordinates), leaving

$$\int_V \mathbf{B}^\mathrm{T}\boldsymbol{\sigma}\mathrm{d}V = \int_S \mathbf{N}^\mathrm{T}\mathbf{t}\mathrm{d}S + \int_V \mathbf{N}^\mathrm{T}\mathbf{b}\mathrm{d}V \tag{3.29}$$

Introducing elasticity with the use of the constitutive matrix, $\mathbf{D}$, that maintains linearity between stresses and strains

$$\boldsymbol{\sigma} = \mathbf{D}\boldsymbol{\varepsilon} - \mathbf{D}\boldsymbol{\varepsilon}_0 \tag{3.30}$$

where ε_0 contains the initial strains. With the kinematic relation for elastic strains, (3.30) becomes

$$\boldsymbol{\sigma} = \mathbf{DBa} - \mathbf{D}\boldsymbol{\varepsilon}_0 \tag{3.31}$$

Thus, (3.29) may be rewritten as

$$\left(\int_V \mathbf{B}^\mathrm{T}\mathbf{DB}\mathrm{d}V\right)\mathbf{a} = \int_S \mathbf{N}^\mathrm{T}\mathbf{t}\mathrm{d}S + \int_V \mathbf{N}^\mathrm{T}\mathbf{b}\mathrm{d}V + \int_V \mathbf{B}^\mathrm{T}\mathbf{D}\boldsymbol{\varepsilon}_0\mathrm{d}V \tag{3.32}$$

Also rewriting the boundary conditions, that are stated either as an essential boundary condition in the form of a prescribed displacement vector, $\mathbf{u}$, or by a natural boundary condition in the form of the traction vector, $\mathbf{t}$, as mentioned above, into

$$\mathbf{t} = \mathbf{Sn} = \mathbf{h} \qquad \text{on} \quad S_h$$
$$\mathbf{u} = \mathbf{g} \qquad \text{on} \quad S_g \tag{3.33}$$

in the meaning that $\mathbf{t}$ is known on the boundary S_h and $\mathbf{u}$ is known on the boundary S_h, enables us to state the FE formulation for three dimensional elasticity as

$$\left(\int_V \mathbf{B}^\mathrm{T} \mathbf{D} \mathbf{B} \mathrm{d}V \right) \mathbf{a} = \int_{S_h} \mathbf{N}^\mathrm{T} \mathbf{h} \mathrm{d}S + \int_{S_g} \mathbf{N}^\mathrm{T} \mathbf{t} \mathrm{d}S + \int_V \mathbf{N}^\mathrm{T} \mathbf{b} \mathrm{d}V + \int_V \mathbf{B}^\mathrm{T} \mathbf{D} \boldsymbol{\varepsilon}_0 \mathrm{d}V \tag{3.34}$$

To obtain a more compact form of the formulation, the following matrices are established:

$$\mathbf{K} = \int_V \mathbf{B}^\mathrm{T} \mathbf{D} \mathbf{B} \mathrm{d}V \tag{3.35}$$

$$\mathbf{f}_b = \int_{S_h} \mathbf{N}^\mathrm{T} \mathbf{h} \mathrm{d}S + \int_{S_g} \mathbf{N}^\mathrm{T} \mathbf{t} \mathrm{d}S \tag{3.36}$$

$$\mathbf{f}_l = \int_V \mathbf{N}^\mathrm{T} \mathbf{b} \mathrm{d}V \tag{3.37}$$

$$\mathbf{f}_0 = \int_V \mathbf{B}^\mathrm{T} \mathbf{D} \boldsymbol{\varepsilon}_0 \mathrm{d}V \tag{3.38}$$

so that

$$\mathbf{Ka} = \mathbf{f}_b + \mathbf{f}_l + \mathbf{f}_0 \tag{3.39}$$

where $\mathbf{K}$ is the stiffness matrix, $\mathbf{f}_b$ is the boundary vector, $\mathbf{f}_l$ is the load vector and $\mathbf{f}_0$ is the initial strain vector. Further simplification may be done by having only one force vector:

$$\mathbf{f} = \mathbf{f}_b + \mathbf{f}_l + \mathbf{f}_0 \tag{3.40}$$

which leaves us with the standard FE formulation:

$$\mathbf{Ka} = \mathbf{f} \tag{3.41}$$

3.3.3 Plane Strain

A state of plane strain occurs in thick geometries, i.e. when e.g. the dimension in the z-direction is much larger than in the x- and y-direction and the loading acts in the xy-plane without variations in the z-direction. In this case the only non-zero strains are ε_{xx}, ε_{yy} and γ_{xy}, thus making it a two-dimensional problem. When no initial strains are present, the following relation describes plane strain condition:

$$\begin{bmatrix} \sigma_{xx} \\ \sigma_{yy} \\ \sigma_{xy} \end{bmatrix} = \frac{E}{(1+\nu)(1-2\nu)} \begin{bmatrix} 1-\nu & \nu & 0 \\ \nu & 1-\nu & 0 \\ 0 & 0 & \frac{1}{2}(1-2\nu) \end{bmatrix} \begin{bmatrix} \varepsilon_{xx} \\ \varepsilon_{yy} \\ \gamma_{xy} \end{bmatrix} \tag{3.42}$$

4 FE Modelling

4.1 Software

Altair Engineering's HyperWorks 11.0 CAE simulation software platform was used for all the finite element analyses. The pre-processor, where the model parameters (global geometry, materials, loads, mesh and local shape variables) are defined is called HyperMesh. In HyperMesh, there is a tool called HyperMorph, which was used to model the different shapes. It has a number of different functions. In this project, the function used was the "map to geometry" function. This means that terrain shapes were applied by mapping a set of nodes, defined by a domain, to a line (2D) or a surface (3D), that was drawn independently of the mesh. The process is automatic, and it does not change the number of elements, it only stretches or compresses them. The shapes obtained from mapping the nodes to a line or a surface can be saved and applied by a positive of negative factor. Warnings occur if the mapping creates poor elements (in terms of negative jacobians, exaggerated skew angles, warping, etc.).

The solver used was RADIOSS Bulk Data Format. For the frequency response studies, it was implemented in HyperStudy, which is a design, study, optimization and stochastic study software. Post-processing was done in HyperView (for visualization) and HyperGraph (for plotting curves in diagrams).

HyperMesh was run with a graphical user interface on a PC and so was HyperStudy. However, for solution of large FE models (3D-modeling) where high computational performance is crucial, RADIOSS was run independently of HyperStudy in batch mode on the high performance computing cluster Platon at the computing center Lunarc, Lund University.

4.2   2D Modelling

4.2.1   Geometry and Elements

The 2D model was created as an extracted sheet of the soil profile located where MAX IV will be built. The elements used were four-noded linear elements. In the present setup, they have 2 translational degrees of freedom per node (in the xz-plane). With the application of plane strain in RADIOSS, the shell thickness can be used to scale the load (with an inverse proportional relation). It was thus set to 1 m. The element size was set to 2 x 2 m^2 in order to be capable of describing the shapes in a proper way. The same element size was used throughout the 2D model.

In analogy to the 3D model, the orientation was such that the x-axis was the horizontal axis with its origin in the loading point and positive direction towards the evaluation point (see Figure 4.2).

The global dimensions of the model were difficult to determine, since the earth crust in a relative perspective could be regarded as infinite in width and depth. In some finite element analysis (FEA) solvers, this infinity may be defined by special elements on the boundary that integrates to infinity, and thus creates what is denoted a quiet boundary in terms of wave propagation, with very limited reflections. As such elements were not yet implemented in the solver used, a too small model could provide questionable response as the vibration induced waves would reflect on the boundary. On the other hand, a too large model require a lot of computational power making the calculations very time consuming.

A proposed solution to this was to have elements on the boundary with the length of one fourth of the present wave length and increased damping in order to damp out the waves at the boundary. But as the FE runs performed were frequency sweeps, the wave length obviously varies significantly. Thus, the solution was to extract a reference response from a very large model (2000 m wide and a depth of the bedrock of 1000 m). With loading always applied in the middle of the surface of the models and the response extracted at a distance of 100 m from the loading point, an iteration into smaller and smaller models where the RMS vertical displacement response at the evaluation point for an unscaled frequency sweep between 5–30 Hz with steps of 0.5 Hz was performed. The criterion for the models in order to be investigated further was that their RMS vertical displacement response had to be within $\pm$ 5 % of the large reference model. The results are presented in Table 4.1. (Note that the dimensions stated in Table 4.1 are the dimensions of the bedrock. There is an additional 14 m of clay on top of the bedrock.)

The responses for some relevant models tested are plotted between 5–20 Hz in Figure 4.1. The choice of limiting all runs to an upper level of 20 Hz was done as a result of the very low displacement amplitudes above this level. This was seen both in the values presented by NGI (see section 2.2 and test runs that were performed).

It was obvious that the 540 x 200 m^2 model differed more than the others at low frequencies compared to the reference model (2000 x 1000 m^2). Knowing that the 600 m wide model with a depth of 180 m had an RMS displacement that differed more than 5 % of the reference model, a choice of using the 600 x 160 m^2 (which was indeed within the 5 % limit) was not motivated. Furthermore, the 560 x 200 m^2 model had a more corresponding response at lower frequencies and was thus the best choice.

Table 4.1: Model size convergence analysis.

| Model size [m^2]	$u_{\mathbf{RMS,vert}}$ [m]	Length	Depth	OK?
2000 x 1000	1.19E-10	Start	Start	
800 x 300	1.17E-10	Decreased	Decreased	Yes
600 x 300	1.23E-10	Decreased	Unchanged	Yes
600 x 200	1.23E-10	Unchanged	Decreased	Yes
500 x 200	1.34E-10	Decreased	Unchanged	No
600 x 160	1.14E-10	Increased	Decreased	Yes
600 x 180	1.28E-10	Decreased	Increased	No
560 x 200	1.24E-10	Decreased	Increased	Yes
540 x 200	1.27E-10	Decreased	Unchanged	No
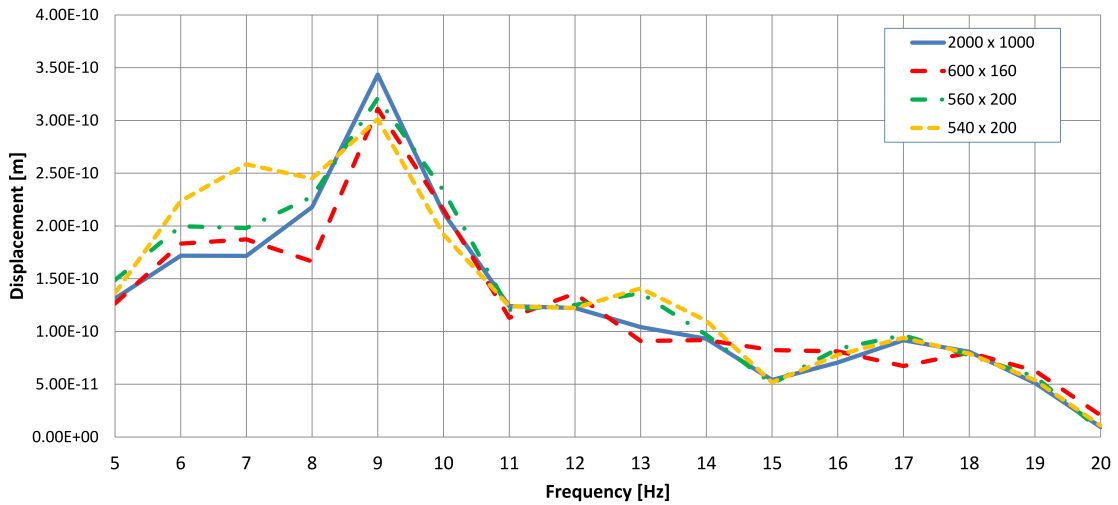
Figure 4.1: Comparison of proposed 2D FE models. Bedrock dimensions stated as width by depth in meters, plus 14 m of covering clay.

The final 2D model had a CPU time of approximately 1.7 % of the reference model and a total of 29,960 elements containing 60,696 degrees of freedom.

4.2.2   Loading, Boundary Conditions and Output

Harmonic unit loading (1 N) was applied in the middle of the top surface on the model and frequency sweeps were performed between 5–20 Hz in steps of 0.5 Hz. The response was extracted at a point 100 m from the loading point, as this is the approximate distance from the highway, E22, to the main building of MAX IV. For closer interpretation, see Figure 4.2. Due to the applied plane strain property, the loading of one node should be interpreted as a line load.

The FE model had no explicitly applied boundary conditions, implying that the boundary condition can be stated as a net zero force condition. The only output from the 2D FE analyses was displacements.
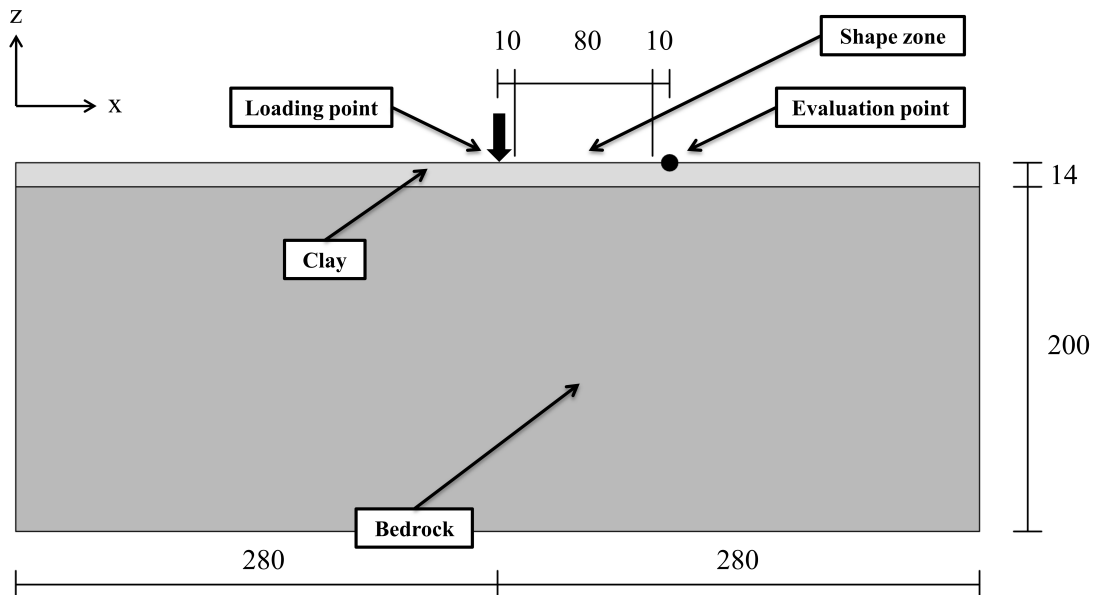
Figure 4.2: 2D model explained. Dimensions stated in meters.

4.2.3   Applied Shapes
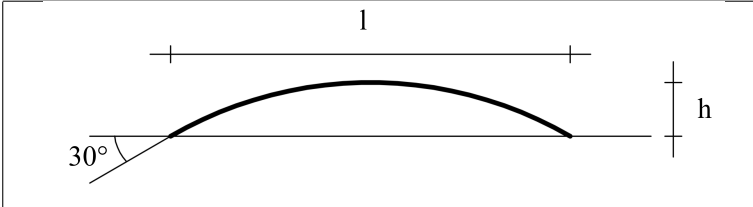
Shapes were applied to the model in a zone starting at x = 10 m and ending at x = 90 m, i.e. 10 m before the evaluation point, creating an 80 m long zone (see Figure 4.2).

There is an infinite number of shapes that might have been interesting to investigate in terms of their vibration reducing properties. A limitation had to be made, and in this project the choice was to mainly investigate shapes in the form of arcs with constant curvature. This was done knowing that a similar approach is the desired solution at MAX IV. Furthermore, it was a very suitable solution when using the

HyperMorph tool (please refer to section 4.1), as using e.g. shapes with sharp corners would often cause poor element quality when mapping the nodes.

The maximum slope angle of the soil was 30° (see section 2.1.1), and for an arc with constant curvature, the 30° slope angle would obviously be at its start- and ending point. A total of 6 different arcs were used to create shapes in the terrain. These were derived from the length of the area where shapes were applied and are denoted 2DShape1–2DShape6, with 2DShape1 implying that it is a two dimensional geometry with one arc stretching over the entire 80 m zone, 2DShape2 implying that 2 arcs cover the zone, and so on. The dimensions of the arcs are presented in Table 4.2.

Table 4.2: Shape dimensions.

Shape notation	Number of arcs	l [m]	h [m]
2DShape1	1	80.00	10.72
2DShape2	2	40.00	5.36
2DShape3	3	26.67	3.57
2DShape4	4	20.00	2.89
2DShape5	5	16.00	2.14
2DShape6	6	13.33	1.79

Furthermore, the application of shapes was done in a uniform manner, implying that when e.g. 2DShape4 was applied, it was applied throughout the shape zone in the form of 4 arcs. In order to denote in which direction the shapes curves (up or down), an extension was added to the stated shape notation: 2DShapeX[Y_Y_..._Y]. The Y's are either 1 or –1, where 1 implies that the arc curves up and –1 that it curves down. Two basic configurations of the arcs were applied, which in the case of 4 arcs would be 2DShape4[1_–1_1_–1] and 2DShape4[1_1_1_1]. These basic configurations were applied with a global shape factor that varies from –1 to 1 in steps of 0.25. This called for yet an addition to the notation, so that when required, the global shape factors were as prefixes to the shapes, e.g. [–0.75]2DShape4[1_1_1_1]. Examples of configurations are shown in Figures 4.3–4.4.

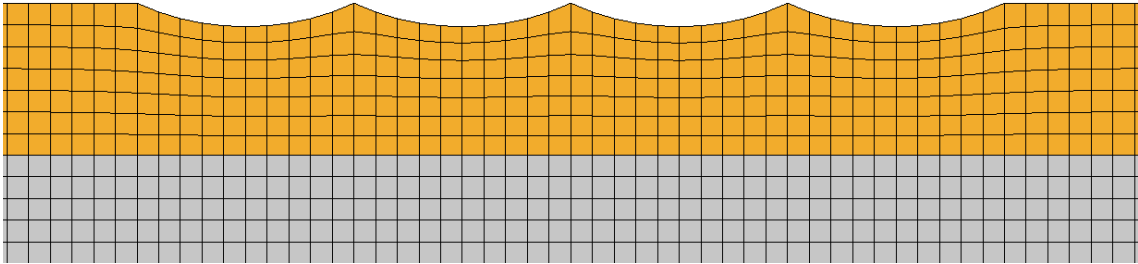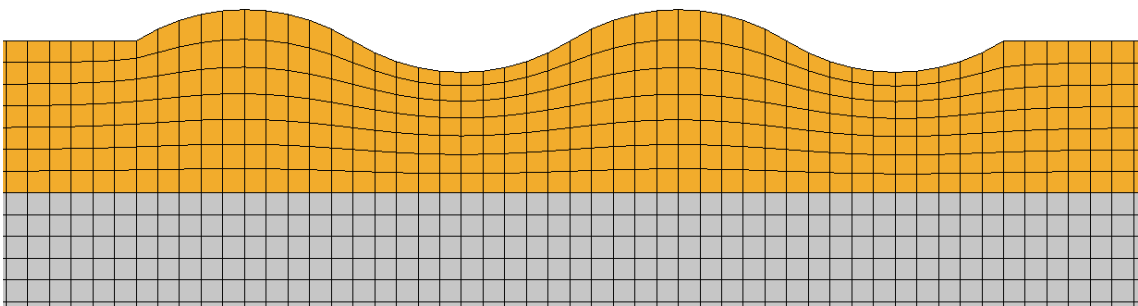**Figure 4.3:** [–0.75]2DShape4[1_1_1_1].

Figure 4.4: [1]2DShape4[1_–1_1_–1].

4.3 3D Modelling

4.3.1 Geometry and Elements

The choice of geometry for the 3D model was done in a slightly less analytical manner than in the case of the 2D model. Due to the significant time needed to perform an analysis (the final model required approximately 10 hours to calculate the response of 7 frequencies using 4 CPU's on a high performance computing cluster), a refined iteration like the one done for the 2D model would be too time consuming. The procedure of determining the 3D model geometry was rather based on a few test models, where the visual verification of a proper wave propagation at relevant frequencies within an area that extended the evaluation point was decisive.

The x- and z-directions in the 3D model corresponded to the ones presented for the 2D model, with the origin placed in the loading point in the middle of the surface of the model (see Figure 4.7). The additional y-axis runs transversally. A six-sided solid element with 8 nodes and 3 degrees of freedom per node was used.

Initially, a choice was made to use a geometry that is symmetrical in x- and y-direction, to obtain a symmetrical response which is obviously more predictable in terms of reflections. Secondly, the fact that loading was applied in one node at the center of the surface (as a point load), implied that the dimensions could be inferior to those of the 2D model, as the waves would be damped out in three dimensions, as opposed to the 2D model, where waves spread only in the plane of the model. A cylindrical model was tested for its more predictable behaviour in terms of reflections on the horizontal boundary. However, as the meshing of a circle creates a less regular mesh (in some part of the model), this solution was not followed up, due to the less predictable mapping of nodes when applying the shapes (which were applied over the whole transversal length of the model).

Ultimately, the choice of geometry for the 3D analyses was a 400 x 400 m^2 surface that was extracted into a 14 m deep layer of clay covering a 100 m deep layer of bedrock. Vertically (z-direction), 2 m deep elements were used for the clay, wheras the bedrock was modeled with an initial 32 m deep layer with an element depth of 4 m (measuring from the top down). This was followed up by a 36 m deep layer of 6 m deep elements and a 32 m deep layer of 8 m deep elements. There was also a partitioning of the element sizes in the horizontal direction. As mentioned, this was meshed symmetrically in x- and y-direction. Measuring from the center of the surface, 2 m long elements were used in a 120 m long zone, followed by zones of increasingly larger elements (16 m of 4 m long elements, 24 m of 6 m long elements and 40 m of 10 m long elements). This was done in order to decrease the CPU-time. Higher frequency loads induce waves with shorter wavelengths that demand a finer mesh for the wave propagation to be modeled properly, but are damped out faster than the lower frequency waves, hence the increase in element size. Vertically, the

elements were deeper in the bedrock, since the wavelengths are longer in the stiffer material.

The final 3D mesh had a total of 518,400 elements containing 1,915,285 degrees of freedom and is shown in Figures 4.5–4.6.
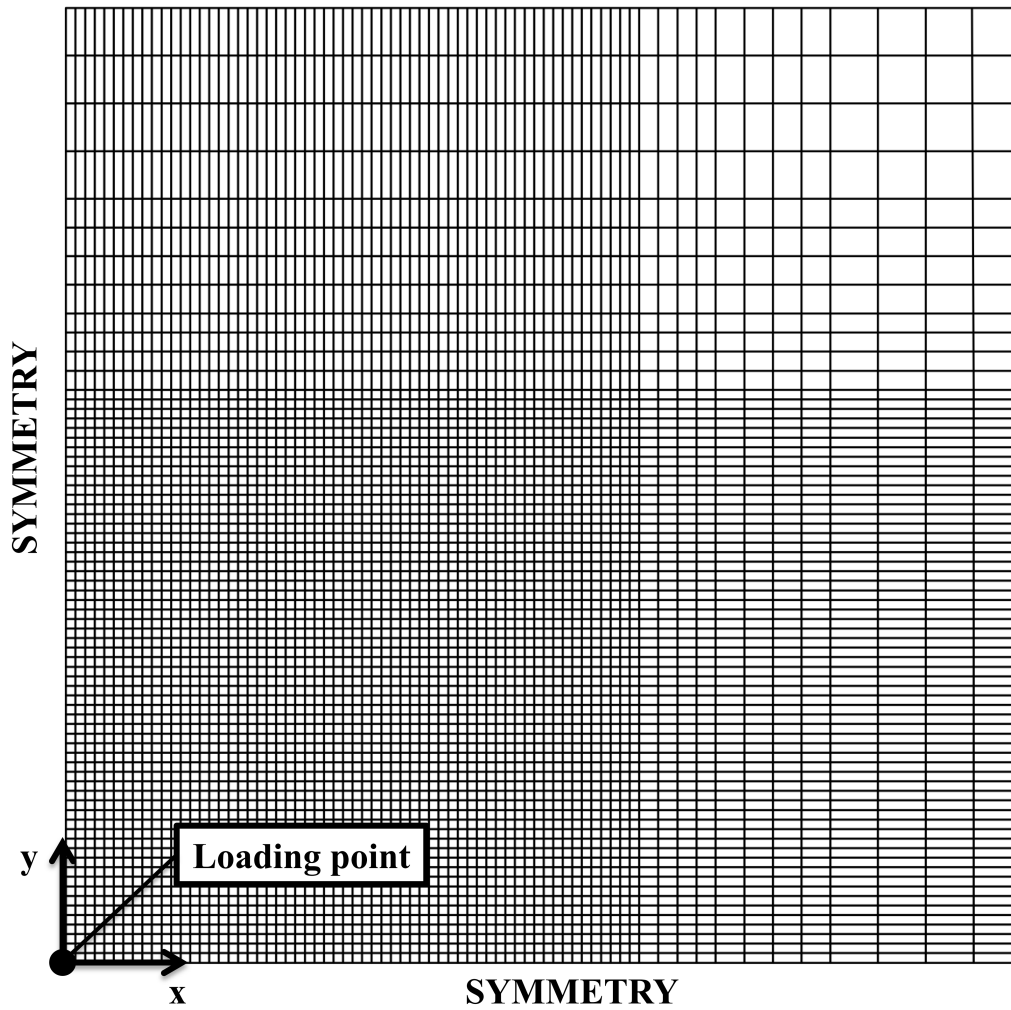
Figure 4.5: View of one quarter of the 3D model top surface mesh (xy-plane).
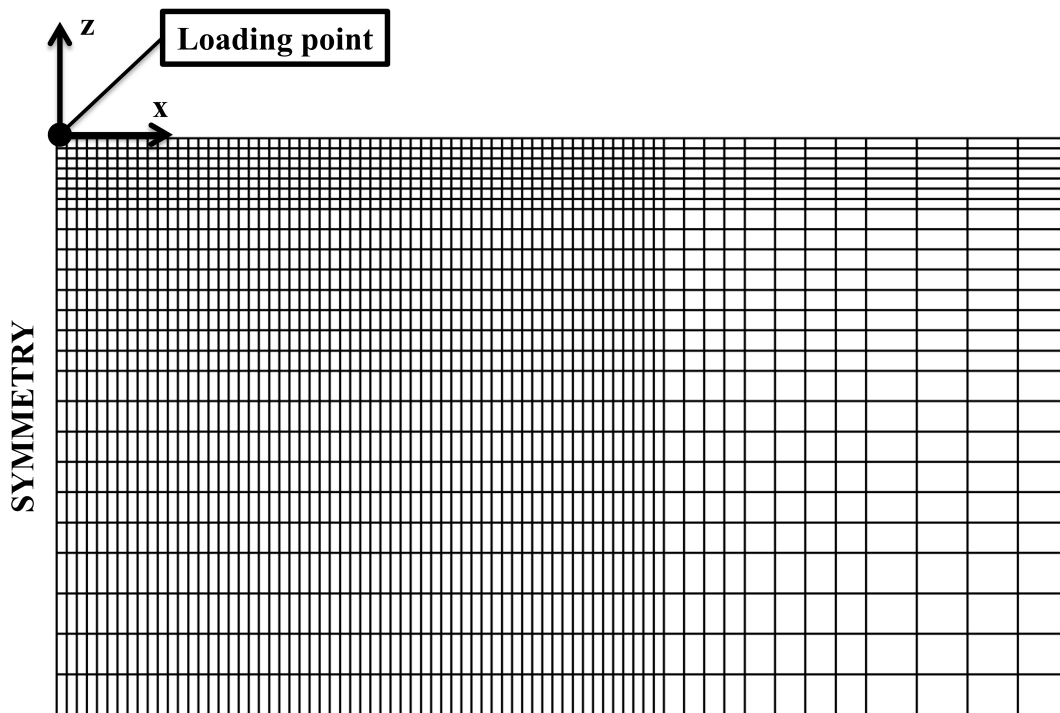
Figure 4.6: View of half of the 3D model vertical side surface mesh (xz- alt. yz-plane).

4.3.2 Loading, Boundary Conditions and Output

Harmonic unit loading was applied to one node in the center of the surface of the model, and the main evaluation point was located on a straight line 100 m horizontally in the x-direction from the loading point. Due to the complexity of the 3D analyses, an additional set of 10 evaluation points, located on a straight line perpendicular to the loading point–main evaluation point line was established (y = ±50 m), see Figure 4.7. A frequency sweep was performed with one third octave bandwidth frequencies of 5.0; 6.3; 8.0; 10.0; 12.5; 16.0 and 20.0 Hz. With the logarithmic scale, a finer sampling of frequencies was obtained in the frequency span where the largest magnitude displacements occur.

A zero net force on the boundaries was set as boundary condition. The only output generated from the 3D analyses was displacements.

4.3.3 Applied Shapes

In analogy to the 2D model, shapes were applied to the 3D model in an 80 m long zone that started 10 m from the loading point and ended 10 m before the
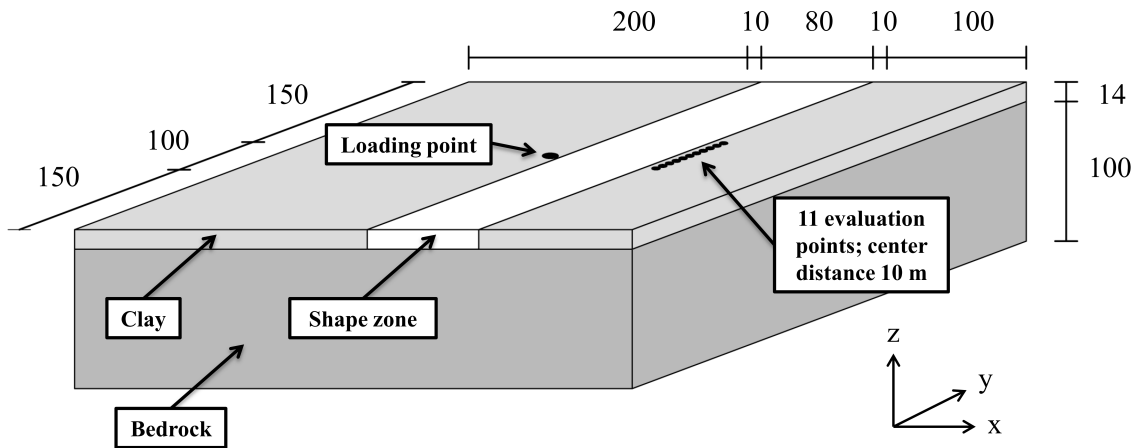
Figure 4.7: 3D model explained.

evaluation point. Shapes were applied over the whole width of the model, according to Figure 4.7. 3D analyses were only performed with global shape factors of 1 and –1. All shapes were derived from the arcs established in the 2D analyses (see section 4.2.3) and as a result of the responses that were seen in these analyses (see section 5.1), only shapes based on 2DShape2, 2DShape3 and and 2DShape4 arcs were analysed. Thus, the height difference in the 3D shapes spanned from 2.89 m to 10.72 m. Three different layouts of 3D shapes were analysed; straight 3D shapes, horizontally rotated 3D shapes and checkered 3D shapes.

Straight 3D Shapes

The initial shapes applied to the 3D model were 3D versions of the 2D shapes, i.e. the arcs were extruded to cover the width of the 3D shape zone. Examples of the straight shape applications and notations are shown in Figures 4.8–4.9.
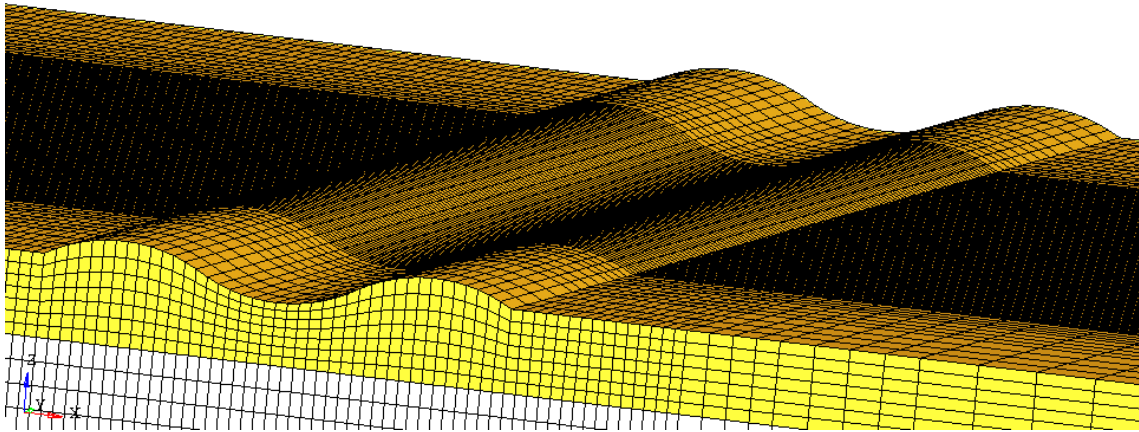
Figure 4.8: [1]3DShape3[1_–1_1]_Straight.
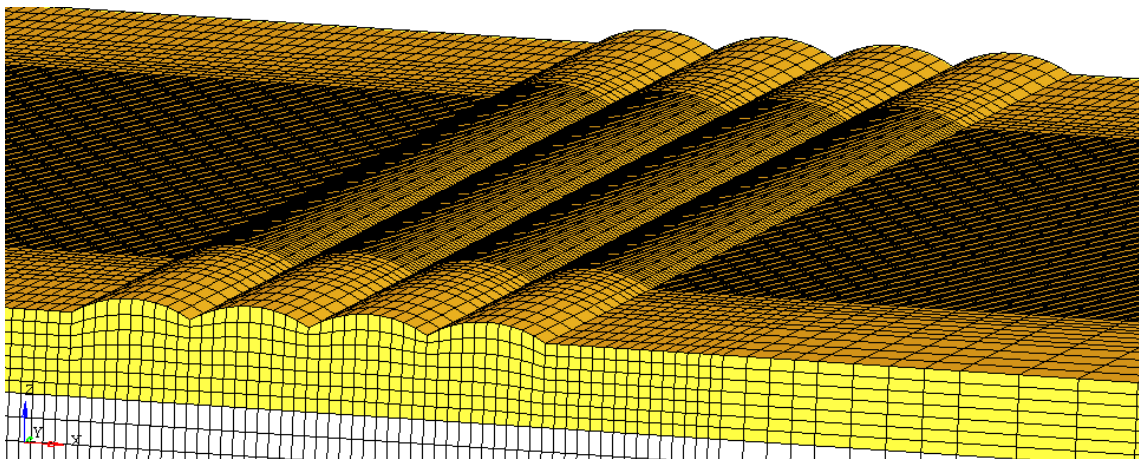
Figure 4.9: [1]3DShape4[1_1_1_1]_Straight.

Horizontally Rotated 3D Shapes

The next shape layout was a version of the straight shape application where the arcs were rotated 45° in the horizontal plane. At the beginning and the end of the shape zone, the extruded arcs were trimmed by the same arcs in their original position (see Figures 4.10–4.11. The denotation and global shape factor would in this case describe the initial direction of the shape at a straight line between the loading point and the evaluation point. As the transversal positioning of the entire shape also matters, an additional notation was added. Only the cases where the x-axis cross in the middle of a hill or valley – or in the transition between a hill or valley – at the beginning of the shape zone were analysed. The former get the suffix, e.g. in the case of 3DShape3, 3DShape3[1_–1_1]_45_Middle and the latter 3DShape3[1_–1_1]_45_RightEdge (where the right edge would be the edge of the shape that starts to the right of the line when moving along the line from the loading point to the evaluation point). The notation should be further interpreted by referring to the

example configurations in Figures 4.10–4.11.
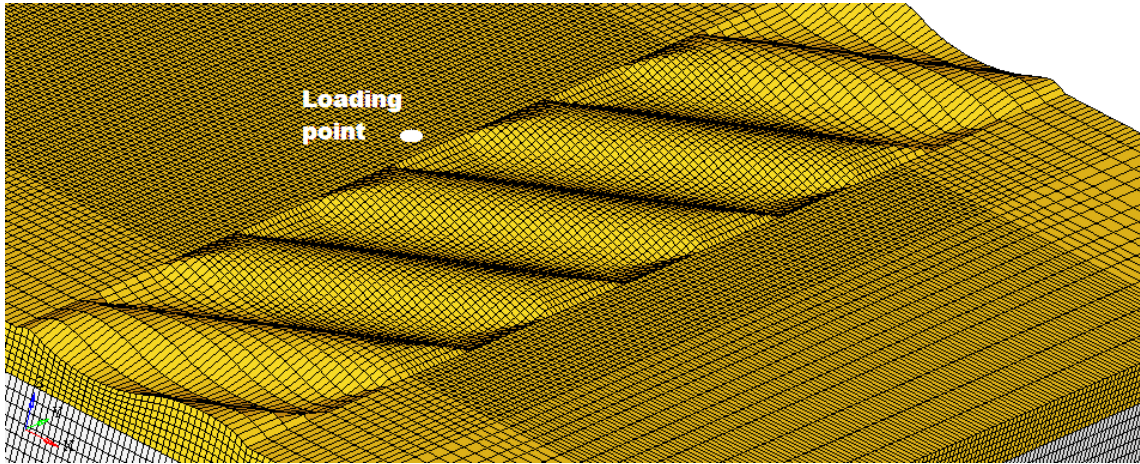
Figure 4.10: [-1]3DShape3[1_–1_1]_45_Middle.
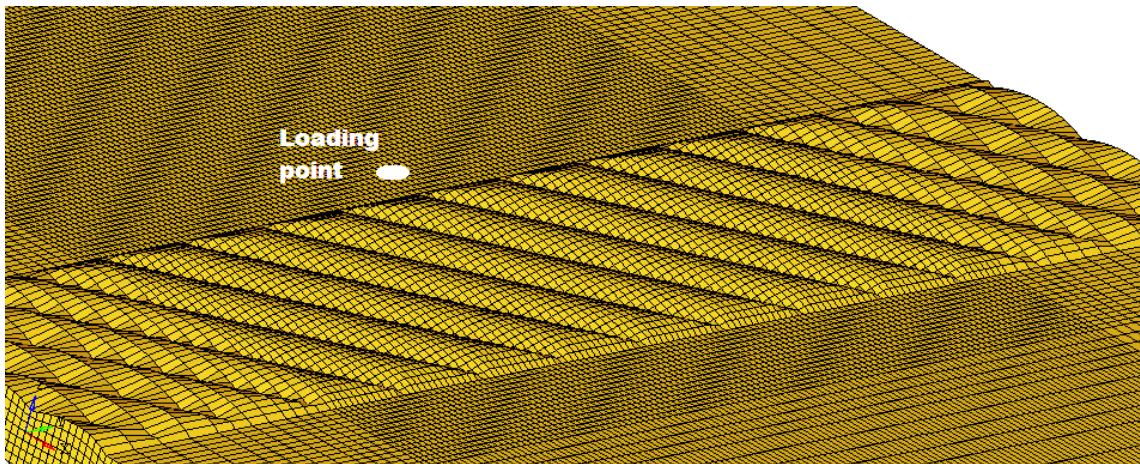
Figure 4.11: [1]3DShape4[1_1_1_1]_45_RightEdge.

Checkered 3D Shapes

Finally, the shape configuration that resembles the solution at MAX IV the most was tested. This was applied as a checkered pattern of hills and/or valleys that were obtained by extracting the intersecting volume of two perpendicularly extruded arcs. The transversal shifting of the pattern was done in analogy to the horizontally rotated 3D shapes. The notation for the checkered pattern is, e.g. for a pattern created by Shape3 arcs with both hills and valleys, 3DShape3[1_–1_1]_Check_Middle alternatively 3DShape3[1_–1_1]_Check_RightEdge. Exemplified configurations with corresponding notation can be seen in Figures 4.12–4.13.
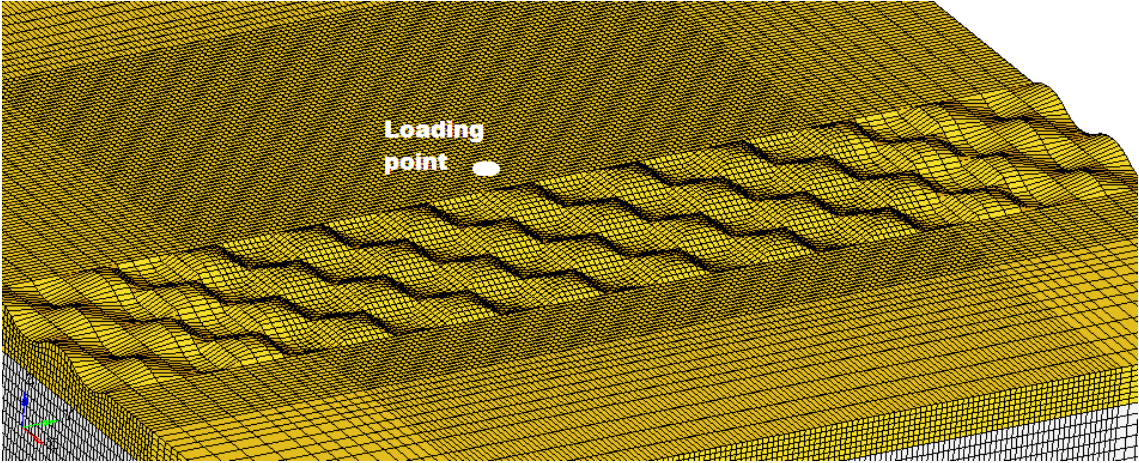
Figure 4.12: [1]3DShape4[1_–1_1_–1]_Check_Middle.
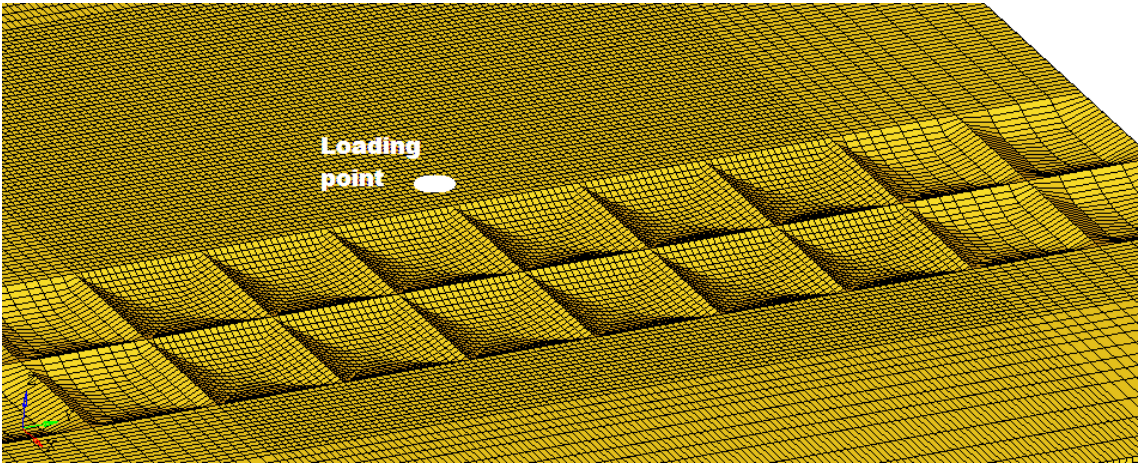
Figure 4.13: [-1]3DShape2[1_1]_Check_RightEdge.

5   Results

5.1   2D Results

In this chapter selected results will be presented, however, complete tabulated results can be found in Appendix A. For a flat configuration, a reference vertical RMS value of $1.55 \cdot 10^{-10}$ m (alternatively denoted 1.55E-10 m in the appendix) was obtained at the main evaluation point.

It could be seen clearly that application of several of the shapes provide results that are beneficial in terms of reducing vibrations. In fact, no shape with two or more hills/valleys that provide a net addition of or no change in material to the shape zone gave an amplification in vertical displacements. With the present setup, the maximum reduction in the RMS value was at 23.4 %. The ten configurations with the best results are presented in Table 5.1.

Table 5.1: The 10 best performing 2D shape configurations.

Shape	$u_{z,RMS}$, [% of flat terrain]
[-1]2DShape2[1_−1]	76.6
[-0.75]2DShape2[1_−1]	79.5
[1]2DShape2[1_−1]	80.0
[-0.75]2DShape1[1]	80.7
[1]2DShape3[1_−1_1]	80.8
[0.75]2DShape2[1_−1]	82.3
[0.75]2DShape3[1_−1_1]	85.0
[-1]2DShape4[1_−1_1_−1]	85.6
[1]2DShape4[1_−1_1_−1]	88.1
[1]2DShape5[1_1_1_1_1]	88.9

The shape that provided the largest reduction in vertical displacements was 2DShape1, for which the results be will presented subsequently. More consistent in their behaviour, and with large reduction in vertical displacements were 2DShape2 and 2DShape3 with altering directions on the arcs, both with a global shape factor of 1 and 0.75. For 2DShape2 this was also the case with global shape factors of −1 and

–0.75, but not for 2DShape3. This is explained by the fact that 2DShape3[1_–1_1] with a negative global shape factor provides a reduction in material in the shape zone (3 being an odd number). It was seen in all 2D configurations with an even number of arcs that are applied in altering directions, that starting out with a valley (i.e. a negative global shape factor) provided a better result – which implies that the positive effect of a hill is increased when it is preceded by a valley rather than the abrupt transition from a flat terrain.

Notable was also the fact that for 2DShape5 and 2DShape6, the configuration that provided the best reduction in vertical displacements at the evaluation point was the one where all arcs curved upwards, which was not the case for 2DShape2–4. For these configurations (2DShape5 and 2DShape6), a negative change in mass (i.e. a negative global shape factor for 2DShape5[1_1_1_1_1], 2DShape5[1_–1_1_–1_1] and 2DShape6[1_1_1_1_1_1]) always lead to an increase in the vertical RMS response (i.e. amplification). This was also the case for 2DShape4[1_1_1_1]. The same tendency could be seen for 2DShape2 and 2DShape3 as well, however for a negative global shape factor of large magnitude, (global shape factor –1 for 2DShape2[1_1] and 2DShape3[1_–1_1]) and global shape factor –0.75 for 2DShape3[1_–1_1]), a reduction was observed. This was interpreted as an effect of geometry rather than mass, as the valleys of 2DShape2 and 2DShape3 leave only a thin layer of clay above the bedrock.

2DShape1 followed the pattern seen above by providing a significant reduction in response for negative global shape factor of large magnitude, whereas for global shape factors of –0.5 and –0.25 it gave a negative response. Less expected was the fact that for positive global shape factors of 0.5–1, 2DShape1 provided an increase in response. This may imply that only adding material is useless without also introducing a variation in geometry.

Responses were also extracted at a point 10 m away from the evaluation point (i.e. 20 m away from the shape zone and 110 m away from the loading point) for all shapes with global shape factors of 1 and –1. This was done as a way of verifying that the responses at the main evaluation point were not results of some local phenomenon. These responses showed the same tendencies as the ones observed in the main evaluation point. Tabulated values can be found in Appendix A.

For the well-performing 2D shapes with a global shape factor of 1 and –1, a frequency plot is presented in Figure 5.1. It can be seen that there is a reduction in vertical displacements mostly throughout the frequency span for both configurations, and it becomes obvious that the difference in performance of 2DShape2[1_–1] with a maximised negative or positive global shape factor occurs at 8.5 Hz. In Figure 5.2 a visualization of the wave propagation of the [-1]2DShape2[1_–1] model at 9.5 Hz is shown. It can be seen clearly that the wave top in the flat area is of larger magnitude than the corresponding one on the far side of the shape, at the evaluation point. It also became visible from the visualization that the shaped area transmits waves into the bedrock, leaving a wave top on the surface that is spread out over a larger

distance with a lower magnitude. A similar effect can be seen for the [1]2DShape3[1_–1_1] configuration – with the difference that waves are not transmitted to the bedrock to the same extent, probably due to the fact that the valleys of 2DShape3 evidently are shallower in the vertical direction than those of 2DShape2.
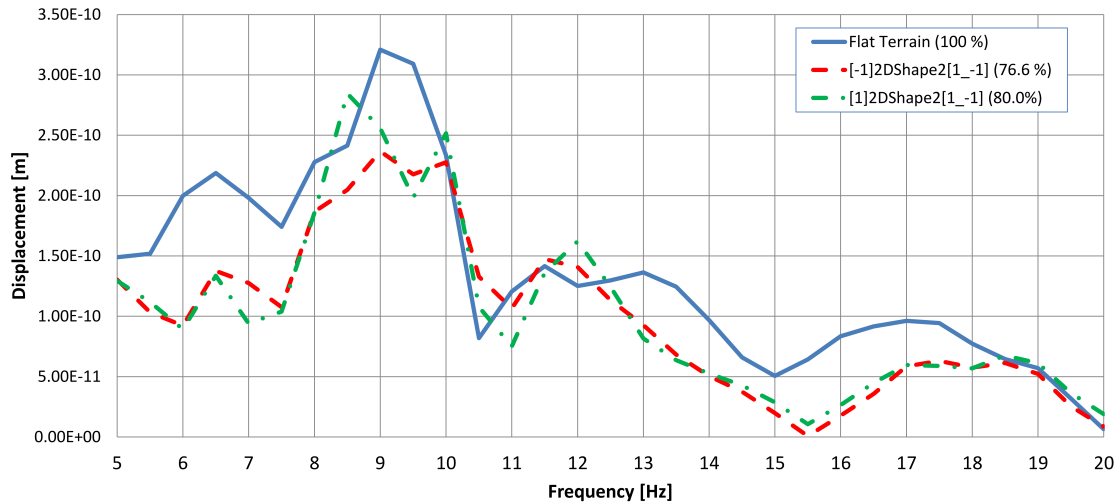
Figure 5.1: 2DShape2 configurations frequency plots.
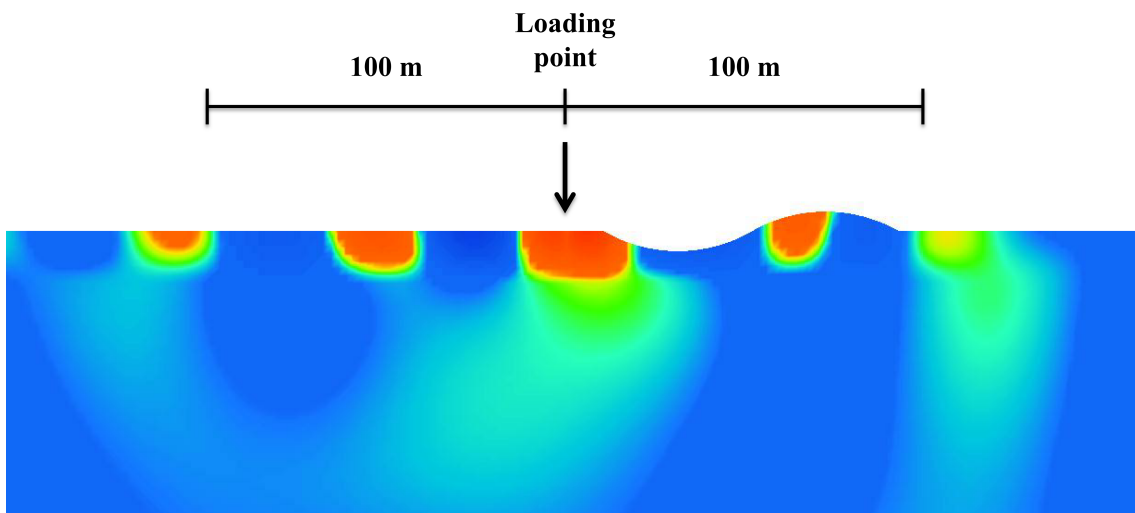
Figure 5.2: [-1]2DShape2[1_–1] vertical displacements magnitude, wavefront behaviour at 9.5 Hz.

For 2DShape4, 2DShape5 and 2DShape6, the plot in Figure 5.3 is representative concerning the differences in performance concerning various configurations of these shapes. 2DShape5, with its odd number of arcs, caused amplification with a negative global shape factor and altering directions on the arcs. 2DShape4 and 2DShape6

performed similarly with a negative and positive global shape factor with altering directions on the arcs, and it can be seen in Figure 5.3 that the reduction in vertical displacements occurs at low frequencies. For the configurations where all arcs curved in the same direction, Shape4, Shape5 and Shape6 got a peak in the magnitude of displacements at 9.5 Hz for a negative global shape factor, whereas a dip occurred at the same frequency for a positive global shape factor.
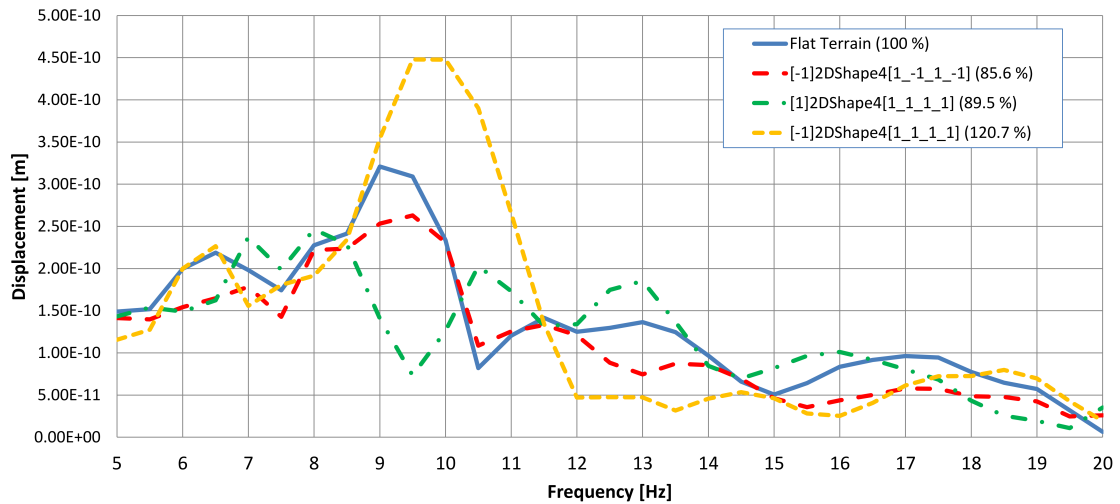
Figure 5.3: 2DShape4 configurations frequency plots.

5.2   3D Results

In this chapter selected results will be presented, however, complete tabulated RMS values of vertical displacements for the 3D shapes may be found in Appendix B. The responses were of approximate magnitude $1 \cdot 10^{-12}$ m, which is logically inferior to the 2D responses due to the difference in loading.

5.2.1   Straight 3D Shapes

For the straight 3D shapes, the results in RMS vertical displacements showed that all configurations, except for the ones where all arcs curve down, provided a positive effect. For[-1]3DShape2[1_1]_Straight a positive effect was also seen in the main evaluation point and four additional evaluation points (at y = ±10 m and y = ±20 m). Further out the results showed an increase in vertical displacements.

Generally, the results were very much according to the 2D results – with the main difference being that even the 3DShape3[1_–1_1]_Straight with a negative global shape factor (i.e. a net negative change in material) provided a positive effect, by decreasing the vertical RMS displacement with 20.3 % in the main evaluation point. As for the 2D results, 3DShape2_Straight provided the largest effect, with a maximum reduction of 25.0 % in the vertical RMS displacement magnitude value at the main evaluation point for the [-1]3DShape2[1_–1]_Straight configuration. Larger reductions are seen in the additional evaluation points with a maximum reduction of ∼30% for the mentioned best performing shape. This is highly interesting, and will be discussed subsequently. However, for comparison with the values presented for the 2D analyses, the main evaluation point provides the most relevant value.

A frequency response function for vertical displacements for some straight 3D shape configurations is presented in Figure 5.4. Just as for the 2D shapes, it seems that 3DShape2_Straight and 3DShape3_Straight behave similarly, whereas the 3DShape4_Straight response to a larger extent resembles the flat terrain response. When looking at the visualizations, Figure 5.5 gives a good picture of what happened when applying the straight 3D shapes (that contain hills). It can be seen clearly that a part of the wave was captured in the first hill and transmitted inside the hill along the y-axis. This phenomenon is the reason why relatively larger reductions were seen in the additional evaluation points – as the wave fronts approaching these points were directed more in the direction of the hill. Ultimately, this was also the reason why hills and valleys rotated 45° in the horizontal plane has been tested in this project – in an attempt of trying to capture the waves to an even larger extent.
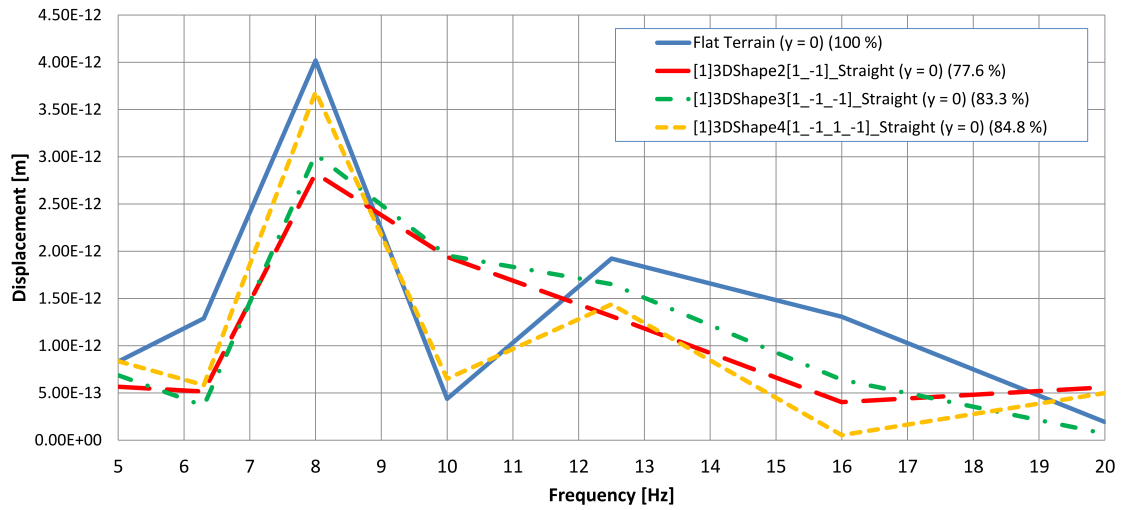
Figure 5.4: Straight 3D shape configurations frequency plot.
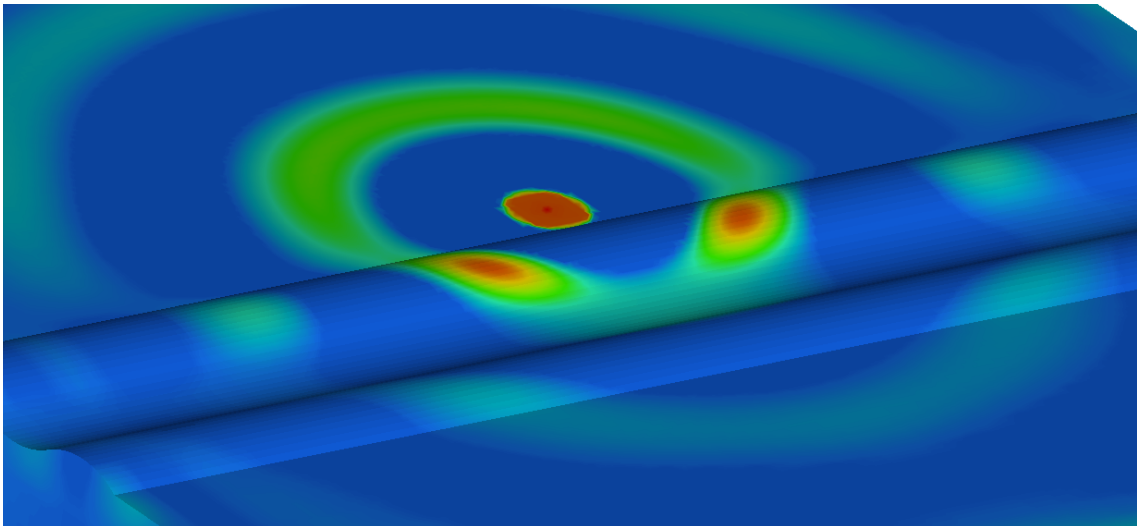
Figure 5.5: [1]3DShape3[1_–1_1]_Straight vertical displacements magnitude, wave behaviour at 8.0 Hz.

5.2.2 Horizontally Rotated 3D Shapes

The 45° horizontally rotated 3D shapes differ from the straight 3D shapes by being non-symmetrical, and thus the responses in the additional evaluation points vary depending on which side of the main evaluation point that is evaluated. This became very obvious for some configurations, as there was a decrease in vertical displacements on one side and an increase on the opposite side compared to a flat terrain. This was the case for e.g. [-1]3DShape2[1_–1]_45_Middle, where the effect is shown in Table 5.2 (with the main evaluation point being located at y = 0).

The diversity in effects was however not unexpected, as the phenomenon of waves being captured inside the hills had already been observed for the straight 3D shapes, and obviously the end of the shape zone looks differently at different additional evaluation points (with some being located where a hill is coming down, some where a valley is coming up and some in the transition between a hill and a valley). The same principle applied to the effects seen by laterally varying the position of the hills and valleys with respect to the loading point. Although the phenomenon of both positive and negative effects in the additional evaluation points were seen to some extent for 3DShape3_45 and 3DShape4_45 as well, the effect was most considerable for 3DShape2_45. This is logical, since the arcs from which the shapes are derived in this case are 40 m long, which in a 45° cut becomes ∼55 m, which is more than half the distance (100 m) of the line from which the additional responses were extracted. Thus, with these dimensions, a large proportion of the area between the loading point and the line on which the evaluation points are located may be only a hill or only a valley.

Table 5.2: 3DShape2[1_–1]_45_Middle RMS vertical displacements effect in additional evaluation points; y = 0 is the main evaluation point.

y [m]	$u_{z,RMS}$, [% of flat terrain]
–50	116.8
–40	127.4
–30	133.8
–20	135.0
–10	120.8
0	88.0
10	52.7
20	41.0
30	50.9
40	71.8
50	85.2

This was exemplified in the case of 3DShape2[1_–1]_45_RightEdge, where a positive global shape factor provided a response that was similar to the one seen in Table 5.2,

whereas a negative global shape factor provided a reduction in the magnitude of approximately 50 % in the majority of the evaluation points – and thus ending up as the best performing shape configuration tested in this thesis. The difference in responses between these two configurations is shown in Figure 5.6 for the main evaluation points. The behaviour of the best performing model is shown in Figure 5.7. Note how the wave tops are captured in the hills.

A negative shape factor to the 45° 3D shapes where all arcs curve in the same direction (i.e. only valleys) always provides a negative result. Applying only hills was positive in all evaluation points except for [1]3DShape4[1_1_1_1]_45_RightEdge, where a small increase in RMS vertical displacements of approximately 2–5 % was observed in half of the evaluation points.

Throughout the tables with results for the horizontally rotated 3D shapes, small groups of evaluation points or even singular evaluation points stood out with particularly poor results in the form of an amplification of the RMS vertical displacements. This is a phenomenon which has been identified to occur at points near where the shape zone ends in the transition between a hill and a valley. The phenomenon is shown in Figure 5.8.
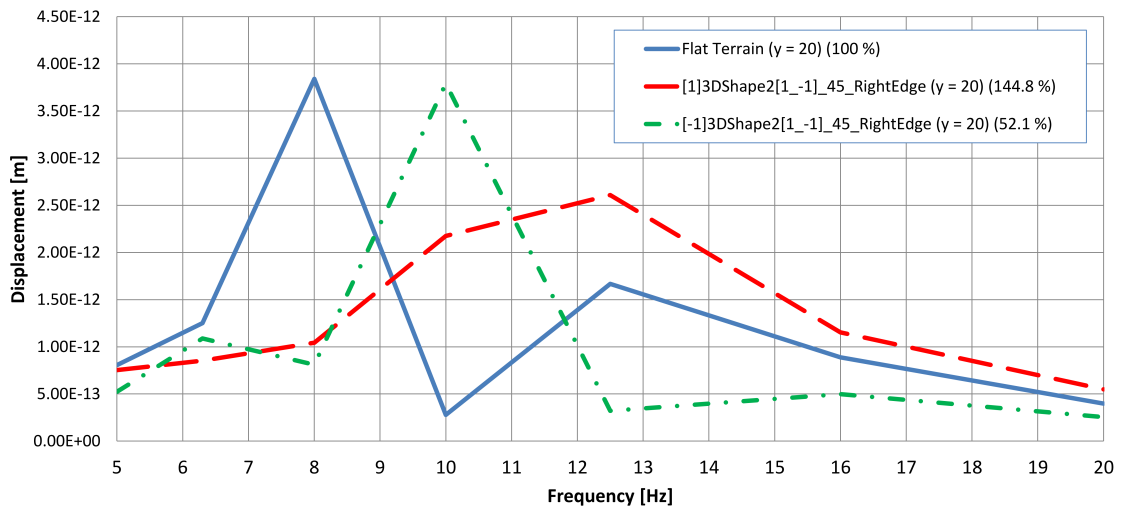
Figure 5.6: 3DShape2[1_–1]_45_RightEdge configurations frequency plot.
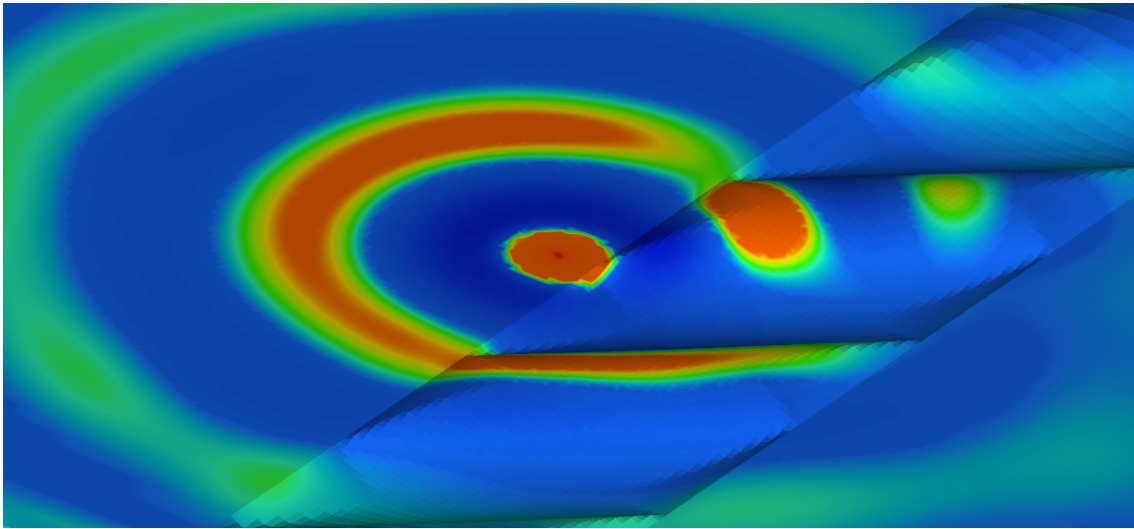
Figure 5.7: [-1]3DShape2[1_–1]_45_RightEdge vertical displacements magnitude, wave behaviour at 8.0 Hz.
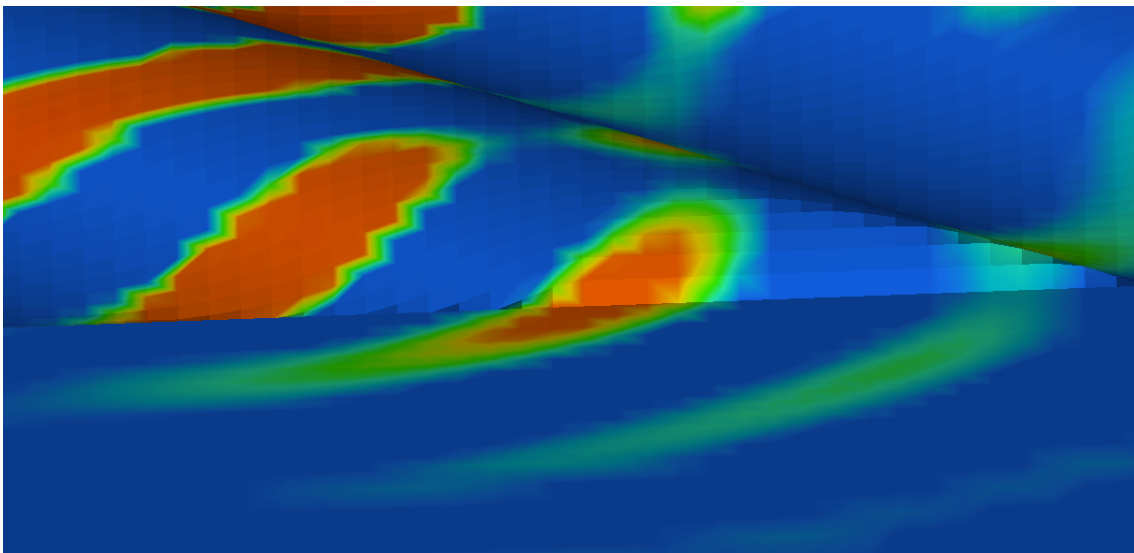
Figure 5.8: Amplification of displacements at transition between hill and valley where the shape zone ends. [1]3DShape3[1_–1_1]_45_RightEdge vertical displacements magnitude, wave front behaviour at 12.5 Hz.

5.2.3   Checkered 3D Shapes

The one clear tendency seen for the other shape layouts applied to the check-
ered one as well: Letting all shapes curve downwards created an increase in ver-
tical displacements in the evaluation points, i.e. a negative effect. Less consistent
with respect to the previously presented shape layout results was the fact that for
3DShape3[1_1_1]_Check_RightEdge and 3DShape4[1_1_1_1]_Check_RightEdge with a
positive global shape factor (i.e. only hills), an increase in vertical displacements
was seen in the main evaluation point and its the closest lying additional evaluation
points. There was indeed an increase in material with higher damping (clay), but
from investigating the visualizations, it seems this did not weigh up for the fact that
applying only hills actually captured the waves in the rows of elevations that oc-
curred in the x-direction (the direction of the line between the loading point and the
main evaluation point) and thus leading the waves towards the middle of the model
on the far side of the shape zone. This effect was not seen for the corresponding
[1]3DShape2[1_1]_Check_RightEdge configuration, where the reduction in vertical
displacements was actually the largest of all the checkered 3D shape configurations
with a reduction of approximately 50 % in the main evaluation point. As it can be
verified from the visualizations, the magnitude of the material added and the size of
this 3DShape2_Check configuration is what causes an increase – since the effect of
capturing the waves in the middle rows of hills is seen even for this configuration.

For the configurations where there is actually a checkered pattern of hills and
valleys, a somewhat opposite effect occurred. Here, all tested configurations of
3DShape4_Check provided a decrease in vertical displacements in all the evaluation
points, whereas some of the configurations derived from the larger arcs lead to an
increase in vertical displacements in some evaluation points. From the visualizations
it can be seen that 3DShape4_Check with both hills and valleys created more obvious
diagonals made up of elevations into which the waves were captured and lead, anal-
ogously to the horizontally rotated 3D shapes. The difference in behaviour between
the 3DShape4_Check with only hills and with both hills and valleys can be seen
in Figures 5.9 – 5.10. The latter provided a reduction in vertical displacements of
around or more than 20 % in the area around the main evaluation point for all of the
different variations of lateral positions of the shapes, which is the same as the best
configurations of the corresponding 3DShape2_Check and 3DShape3_Check config-
urations. Plots of vertical displacements per frequency for two relevant evaluation
points can be seen in Figure 5.11.
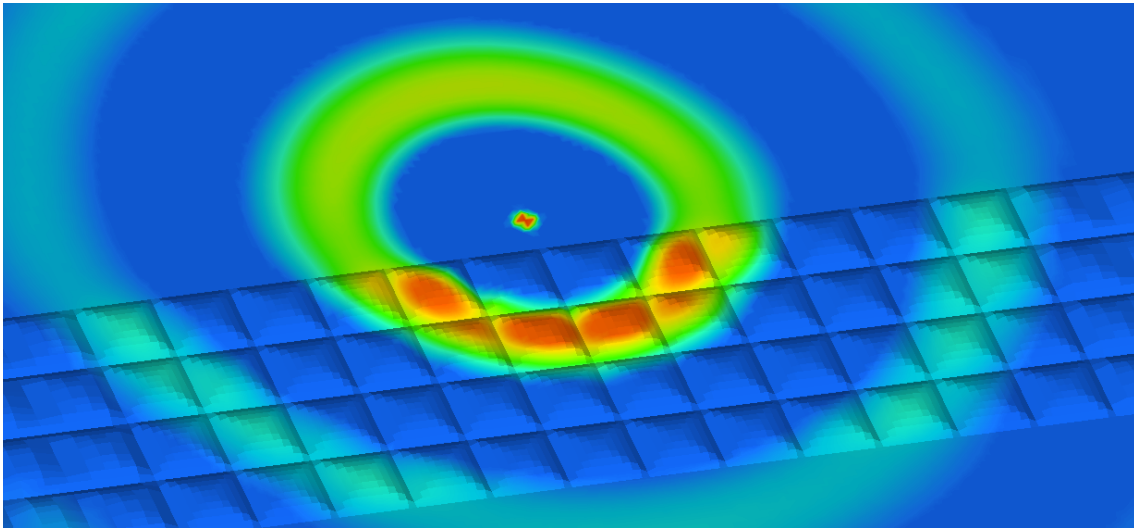
Figure 5.9: [1]3DShape4[1_1_1_1]_Check_RightEdge vertical displacements magnitude, wave behaviour at 8.0 Hz.
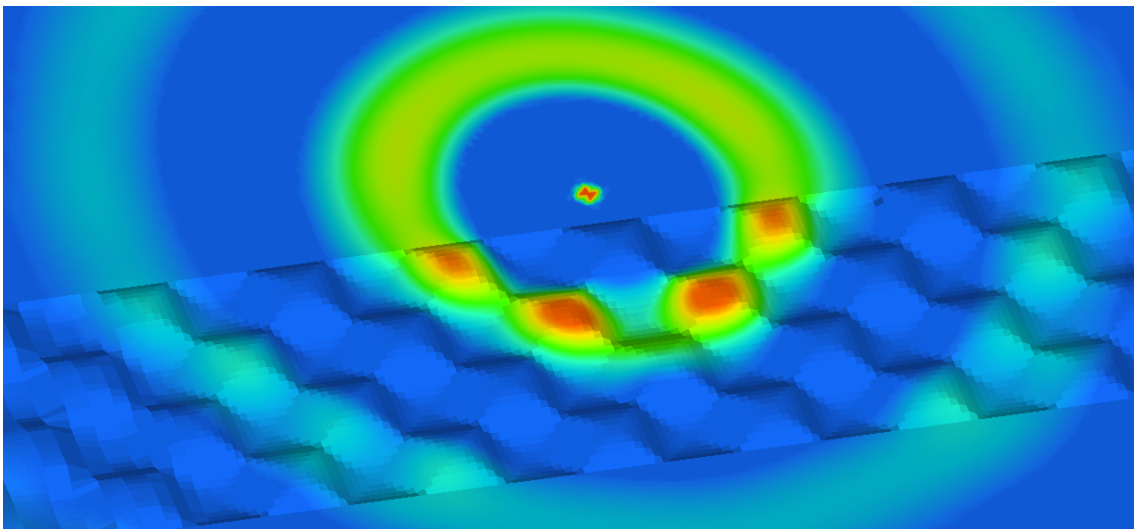
Figure 5.10: [1]3DShape4[1_1_1_1]_Check_Middle vertical displacements magnitude, wave behaviour at 8.0 Hz.
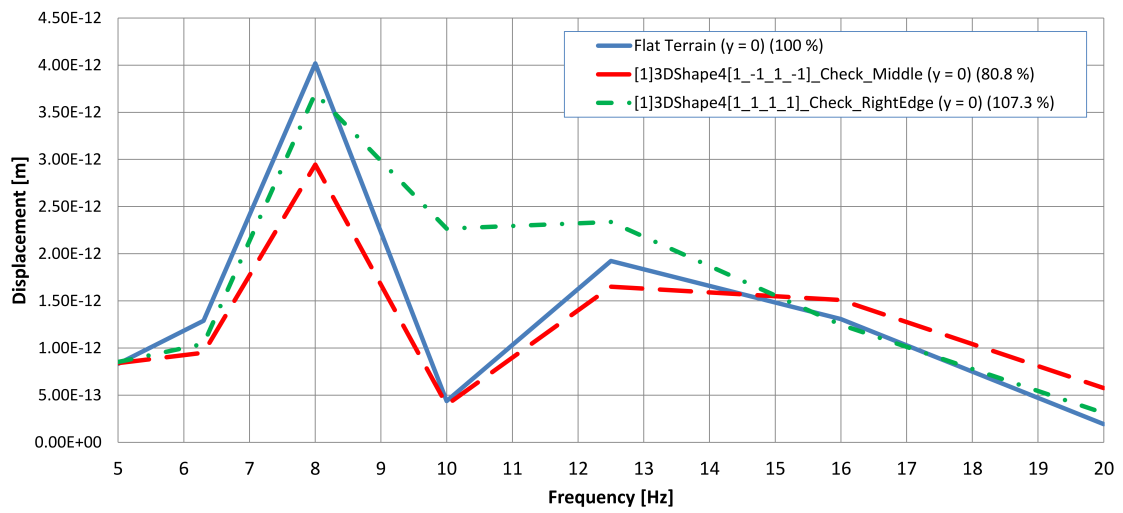
Figure 5.11: 3DShape4_Check configurations frequency plot.

6 Conclusions and Discussion

6.1 Conclusions

As the Results chapter of this thesis is somewhat complex and in detail, the clear tendencies observed in the behaviour of the applied shapes will be briefly summarized in this section.

In two dimensions with plain strain behaviour and harmonic loading (i.e. line loading), the following conclusions may be drawn:

- Applying only valleys or more valleys than hills in an altering manner gives a reduction in RMS vertical displacements when the dimensions of the shapes are sufficiently large (i.e. 2DShape1–2DShape3). Otherwise this is not recommended, as an increase in vertical displacement is observed.

- Applying a shape in the form of altering hills and valleys provides a reduction in RMS vertical displacements for a positive or zero change in mass (the latter implying an even number of hills and valleys).

- Larger sized hills are more efficient in reducing vertical displacements than smaller sized hills.

- If the dimensions are sufficiently large (2DShape2–2DShape4), the smooth transition between a valley and a hill seems to increase the performance of the hill better than the abrupt transition between two hills. Valleys should be present.

- For smaller sized hills (2DShape5–2DShape6), the best solution is applying hills exclusively.

- A reduction in RMS vertical displacement of more than 20 % is seen for the best performing 2D shapes.

In three dimensions with harmonic point loading, the following conclusions may be drawn:

- Digging out valleys exclusively might have a positive effect in terms of reducing vibrations if one digs deep enough. With the dimensions applied in this thesis,

however, applying only valleys generally increases vertical displacements.

- Continuous hills seem to have the ability to capture and direct surface waves in the direction of the hill. This effect depends on the angle in which the waves hit the hill. A larger caption can be obtained by rotating the hills in the horizontal plane in the direction of the waves, and this may provide reductions in vertical dynamic displacements locally of large magnitude (50 % with the setup present in this thesis). However, it should be emphasized that hills that have a longitudinal direction component in the direction of the evaluation point may also, depending on the positioning of the hills, direct waves towards this point and thus increase the vertical displacements. Attention should be payed especially when the transition between continuous hills and valleys are ended and located close to a sensitive area.

- With the application of transversally directed hills and valleys, a reduction of RMS vertical displacements of approximately 20 % can be expected.

- Larger sized hills are more efficient than smaller sized hills.

- The smooth transition between a hill and a valley seems to transmit waves into the hills better than the abrupt transition between two hills. Valleys should be present.

- A regular checkered pattern of hills and valleys work in somewhat the same way as continuous hills, as waves follow the paths of neighbouring elevations (depending on the angle of the path and the direction of the wave). Applying only valleys increase vertical displacements, whereas applying only hills can create a straight path of hills that concentrates and leads the waves the shortest way to the evaluation point, and thus increasing the vertical displacements.

- A checkered pattern of both elevations and depressions where the pattern is finely defined is the ideal. In the case investigated in this thesis, reductions of more than 20 % in RMS vertical displacements were seen around the main evaluation point and its proximity for the smallest elevations and depressions, which obviously create the finest pattern.

6.2   Discussion on Results

A number of conclusions have been drawn in the preceding sections. Would the sum of these be a sufficient incitement to expand the zone of hills and valleys into also covering the area between MAX IV and the passing highway?

The 2D results provided the most confident conclusions, as the derivation of the computational model was carried out in a most satisfying manner and the steps of the frequency sweeps were 0.5 Hz. The intriguing aspect of the 2D analyses was the fact that the loading translated into three dimensions would correspond to a

line load inducing straight wave fronts. It is questionable whether this is applicable when representing passing cars.

Deriving the model used for the 3D analyses was more of a challenge, considering the very long computational time. The challenge was to make the model function at the lower frequencies, where the wavelengths are long. The model seemed to perform well in a zone that extended the evaluation points, but the worry is rather directed towards the relatively large steps in the frequency sweeps. Looking at e.g. Figure 5.6, it can be seen that the flat terrain analysis seems to capture a peak in the response, whereas one of the shape configurations is obviously missing a peak between 8 and 10 Hz. In this particular case a negative effect was not missed, as the configuration mentioned indeed had an RMS vertical displacement that was superior to the flat terrain. However, the flat terrain seemed to capture a similar peak at all evaluation points, whereas the different shapes seemed to significantly affect where a potential peak occurred. It would however demand an unreasonable amount of time to investigate all plots for all evaluation points at all configurations.

A fact that strengthens the conclusions drawn from the 3D analyses in general is that the corresponding 2D and 3D shapes (i.e. the straight 3D shapes) showed similar phenomena and even a similar magnitude of reductions in displacements.

In terms of vertical displacements, the conclusions drawn so far makes for a considerable confidence in recommending that shapes should be extended and applied to a larger area at the MAX IV. Horizontal response were however not analysed at all and is equally severe to the instruments operating at MAX IV. A brief discussion follows in a subsequent section. As will the possibility of scaling the frequency sweep in order to resemble the governing frequencies contained in the actual traffic loading in accordance with section 2.2.

6.2.1 Horizontal Displacements

The effects of how shaping the terrain affects horizontal displacements have not been investigated in this project. The horizontal output from the analyses does exist, but has not been in the scope of this thesis. However, in order to get an idea of the effects horizontally, which might encourage a continued attention to this matter, the reduction in RMS displacement in x-direction from the vertically best performing 2D and 3D shape respectively are presented in Table 6.1. The value for the 3D model is extracted in the main evaluation point, and it should be emphasized that the additional evaluation points show an even larger reduction.

The horizontal reductions of displacements in the x-direction are of reassuring magnitude and could imply that it is reasonable to assume that this could be a general conclusion.

Table 6.1: Horizontal RMS displacements (x-direction) in main evaluation point in vertically best performing shapes.

Shape	$u_{x,RMS}$, [% of flat terrain]
[-1]2DShape2[1_–1]	79.5
[-1]3DShape2[1_–1]_45_RightEdge	71.3

6.2.2   Scaling of Harmonic Load

Initially, the intention was to utilize the measurements performed by Norwegian Geotechnical Institute, presented in section 2.2 for a normative scaling of the load per frequency so that it would contain the governing frequencies of the traffic load. This would have made the results even more relevant to the possible extension of a landscape of hills and valleys at MAX IV. It could have been done by dividing the displacements in Table 2.2 by the corresponding results of an FE analysis where no shapes were applied. In the case of a given frequency:

$$\text{Non-normative scaling factor of load at } x \text{ Hz} = \frac{u_{measured,x}}{u_{FEA,x}} \qquad (6.1)$$

Finally a proportional scaling of these fractions into a number of normative scaling parameters throughout the frequency span could have been applied to the results from the 1 N frequency sweeps. This was also attempted, however, problems occurred when it became clear that the eigenfrequencies obtained from the flat terrain FE runs were slightly shifted compared to the eigenfrequencies of the investigation performed by NGI. A fitting of the curves of the FRFs was also attempted, but as the shifting was not uniform throughout the curve, the results obtained were poor, as the peaks in the curves are very distinct. Thus, the attempt of scaling the load was rejected.

6.3   Further Work on the Subject

As already mentioned, the effects of shaping the terrain on horizontal vibration induced displacements should be followed up. During this project, a lot of time and effort has been put into deriving the geometry of the FE models. This was partly a result of the FE software being new compared to the software that has been used so far by other participants in the work evolving around the vibrations at the MAX IV site. In combination with the number of analyses performed and the large amount of vertical displacements data, the time has not sufficed for the equally important and clearly accessible horizontal analyses.

Where this project has been a general study strongly coloured by the MAX IV conditions, maybe a more specific study on a proposed solution, that does indeed

exist (designed by landscape architects), should be performed. This would effectively bring down the number of variables in the analysis, opening up for a more finely tuned analysis (e.g. smaller frequency steps in the 3D analysis) and possibly new interesting variables. The location of the harmonic load could be an example (i.e. the transversal placing of the shapes), as great differences has been seen when shifting the placing of the transversally non-homogeneous shapes in steps of a quarter of the repetitive phase. One might also pose the question whether harmonic unit loading with a steady-state output simulates cars passing by in a satisfactory manner. Maybe simulating cars in the form of a transient moving load would be interesting.

With a proposed and fixed solution in terms of shapes, it would also be interesting to introduce a variable in the form of materials. In this project, the existing, rather stiff (from pre-consolidation) clay has been used to create the shapes in the landscape. It has become clear that the material that will be used in reality for the shapes on the MAX IV site is a mix of the clay (that has been dug up and thus lost a lot of stiffness) and residue soil material from e.g. nearby farming. A hypothesis is that this softer material will introduce a larger loss factor (damping) and thus contribute to a larger reduction in vibrations. A controlled use of materials in the shapes could possibly be very efficient in this matter.

Bibliography

[1] MAX-lab (2010). *Max-lab web homepage.* Max-lab. http://www.maxlab.lu.se, visited august 2011.

[2] Geoforum (2011). *Sveriges geologi.* Sektionen för geo- och miljövetenskaper, Stockholms universitet. http://www.tellus.geo.su.se/geologi_i_skolan/Pages/sveriges_geologi1.htm, visited 2011-09-30.

[3] Chopra Anil K. (1995). *Dynamics of Structures.* Prentice Hall.

[4] Davidsson Peter (2004). *Structure-acoustic analysis; finite element modelling and reduction methods.* Doctoral Thesis, Division of Structural Mechanics, Lund University Faculty of Engineering.

[5] Pelosi Guiseppe (2007). *The Finite Element Method, Part I: R. L. Courant.* Article in IEEE Antennas and Propagation Magazine, Vol. 49, No. 2, April 2007.

[6] Bell Kolbein (2009). *Store Norske Leksikon: Elementmetoden.* http://snl.no/elementmetoden, visited 2011-10-05.

[7] Andersen Lars (2006). *Linear elastodynamic analysis.* Lecture notes, Aalborg University, Department of Civil Engineering.

[8] Correspondence with contractor PEAB, June 2011.

[9] Correspondence with Norwegian Geotechnical Institute, June 2011.

[10] Axelsson Kennet (2005). *Introduktion till geotekniken.* Institutionen för Geovetenskaper, Uppsala Universitet.

[11] Ottosen N. S. and Petersson H. (1992). *Introduction to the Finite Element Method.* Prentice Hall.

A   Tabulated 2D Results

In this appendix, the RMS vertical displacement for all tested configurations of 2D shapes are presented in the main evaluation point. The flat terrain reference value is found for a global shape factor of 0. Following the tables containing the results for the main evaluation point (x = 100 m), the additional evaluation point (x = 110 m) results, used to verify the results from the main evaluation point, are presented. The latter are only checked for global shape factors of 1 and –1.

Table A.1: 2DShape1 – 2DShape3 results in main evaluation point.

2DShape1[1]									
Global shape factor	-1	-0.75	-0.5	-0.25	0	0.25	0.5	0.75	1
$u_{z,RMS}$ [m]	1.38E-10	1.25E-10	1.61E-10	1.78E-10	1.55E-10	1.49E-10	1.58E-10	1.59E-10	1.57E-10
% of flat terrain	89.0%	80.7 %	104.0 %	114.8 %	100.0 %	96.4 %	102.0 %	102.6 %	101.8 %
2DShape2[1_-1]									
Global shape factor	-1	-0.75	-0.5	-0.25	0	0.25	0.5	0.75	1
$u_{z,RMS}$ [m]	1.18E-10	1.23E-10	1.38E-10	1.50E-10	1.55E-10	1.51E-10	1.40E-10	1.27E-10	1.24E-10
% of flat terrain	76.6%	79.5 %	89.1 %	97.0 %	100.0 %	97.4 %	90.5 %	82.3 %	80.0 %
2DShape2[1_1]									
Global shape factor	-1	-0.75	-0.5	-0.25	0	0.25	0.5	0.75	1
$u_{z,RMS}$ [m]	1.53E-10	1.77E-10	1.79E-10	1.68E-10	1.55E-10	1.46E-10	1.45E-10	1.49E-10	1.48E-10
% of flat terrain	98.8%	114.4 %	115.7 %	108.8 %	100.0 %	94.2 %	94.0 %	96.4 %	95.7 %
2DShape3[1_-1_1]									
Global shape factor	-1	-0.75	-0.5	-0.25	0	0.25	0.5	0.75	1
$u_{z,RMS}$ [m]	1.49E-10	1.51E-10	1.55E-10	1.57E-10	1.55E-10	1.49E-10	1.41E-10	1.32E-10	1.25E-10
% of flat terrain	96.1%	97.4 %	100.2 %	101.2 %	100.0 %	96.6 %	91.1 %	85.0 %	80.8 %
2DShape[3_1_1_1]									
Global shape factor	-1	-0.75	-0.5	-0.25	0	0.25	0.5	0.75	1
$u_{z,RMS}$ [m]	1.93E-10	1.86E-10	1.75E-10	1.64E-10	1.55E-10	1.49E-10	1.47E-10	1.47E-10	1.47E-10
% of flat terrain	124.5%	119.9 %	112.8 %	105.7 %	100.0 %	96.3 %	94.8 %	94.8 %	94.7 %

Table A.2: 2DShape4 – 2DShape6 results in main evaluation point.

2DShape4[1_-1_1_-1]									
Global shape factor	-1	-0.75	-0.5	-0.25	0	0.25	0.5	0.75	1
uz,RMS [m]	1.32E-10	1.41E-10	1.48E-10	1.53E-10	1.55E-10	1.54E-10	1.50E-10	1.44E-10	1.36E-10
% of flat terrain	85.6%	91.3 %	96.0 %	98.9 %	100.0 %	99.4 %	97.1 %	93.2 %	88.1 %
2DShape4[1_1_1_1]									
Global shape factor	-1	-0.75	-0.5	-0.25	0	0.25	0.5	0.75	1
uz,RMS [m]	1.87E-10	1.79E-10	1.70E-10	1.62E-10	1.55E-10	1.49E-10	1.44E-10	1.41E-10	1.38E-10
% of flat terrain	120.7%	115.6 %	110.1 %	104.8 %	100.0 %	96.0 %	93.2 %	91.2 %	89.5 %
2DShape5[1_-1_1_-1_1]									
Global shape factor	-1	-0.75	-0.5	-0.25	0	0.25	0.5	0.75	1
uz,RMS [m]	1.59E-10	1.58E-10	1.57E-10	1.56E-10	1.55E-10	1.54E-10	1.53E-10	1.52E-10	1.49E-10
% of flat terrain	102.5%	102.2 %	101.3 %	100.6 %	100.0 %	99.6 %	99.1 %	98.0 %	96.1 %
2DShape5[1_1_1_1_1]									
Global shape factor	-1	-0.75	-0.5	-0.25	0	0.25	0.5	0.75	1
uz,RMS [m]	1.79E-10	1.72E-10	1.66E-10	1.60E-10	1.55E-10	1.50E-10	1.46E-10	1.42E-10	1.38E-10
% of flat terrain	115.5%	111.3 %	107.2 %	103.4 %	100.0 %	97.0 %	94.2 %	91.7 %	88.9 %
2DShape6[1_-1_1_-1_1_-1]									
Global shape factor	-1	-0.75	-0.5	-0.25	0	0.25	0.5	0.75	1
uz,RMS [m]	1.50E-10	1.52E-10	1.53E-10	1.54E-10	1.55E-10	1.54E-10	1.54E-10	1.52E-10	1.50E-10
% of flat terrain	96.7%	98.1 %	99.1 %	99.7 %	100.0 %	99.8 %	99.3 %	98.2 %	96.8 %
2DShape6[1_1_1_1_1_1]									
Global shape factor	-1	-0.75	-0.5	-0.25	0	0.25	0.5	0.75	1
uz,RMS [m]	1.76E-10	1.70E-10	1.64E-10	1.59E-10	1.55E-10	1.51E-10	1.47E-10	1.44E-10	1.41E-10
% of flat terrain	113.6%	109.8 %	106.2 %	102.9 %	100.0 %	97.4 %	95.1 %	93.0 %	91.0 %

Table A.3: 2D shapes, results in additional evaluation point.

	2DShape1[1]					2DShape2[1_1]		
Global shape factor	-1	0	1					
$u_{z,RMS}$ [m]	1.01E-10	1.36E-10	1.19E-10					
% of flat terrain	74.2 %	100.0 %	86.9 %					
	2DShape2[1_-1]					**2DShape2[1_1]**		
Global shape factor	-1	0	1		-1	0	1	
$u_{z,RMS}$ [m]	1.22E-10	1.36E-10	1.10E-10		1.24E-10	1.36E-10	1.19E-10	
% of flat terrain	89.5 %	100.0 %	80.9 %		91.3 %	100.0 %	87.6 %	
	2DShape3[1_-1_1]					**2DShape[3_1_1_1]**		
Global shape factor	-1	0	1		-1	0	1	
$u_{z,RMS}$ [m]	1.26E-10	1.36E-10	1.12E-10		1.57E-10	1.36E-10	1.27E-10	
% of flat terrain	92.2 %	100.0 %	81.9 %		115.1 %	100.0 %	93.2 %	
	2DShape4[1_-1_1_-1]					**2DShape4[1_1_1_1]**		
Global shape factor	-1	0	1		-1	0	1	
$u_{z,RMS}$ [m]	1.29E-10	1.36E-10	1.22E-10		1.54E-10	1.36E-10	1.23E-10	
% of flat terrain	94.6 %	100.0 %	89.8 %		112.9 %	100.0 %	90.4 %	
	2DShape5[1_-1_1_-1_1]					**2DShape5[1_1_1_1_1]**		
Global shape factor	-1	0	1		-1	0	1	
$u_{z,RMS}$ [m]	1.41E-10	1.36E-10	1.32E-10		1.51E-10	1.36E-10	1.27E-10	
% of flat terrain	103.3 %	100.0 %	97.1 %		110.5 %	100.0 %	92.8 %	
	2DShape6[1_-1_1_-1_1_-1]					**2DShape6[1_1_1_1_1_1]**		
Global shape factor	-1	0	1		-1	0	1	
$u_{z,RMS}$ [m]	1.41E-10	1.36E-10	1.32E-10		1.48E-10	1.36E-10	1.29E-10	
% of flat terrain	103.1 %	100.0 %	97.0 %		108.8 %	100.0 %	94.4 %	

B Tabulated 3D Results

The 3D analyses results are presented in this appendix. Each shape has a dedicated table that includes the results for all tested configurations. All the straight shapes are presented first, followed by the horizontally rotated straight shapes, and finally the checkered shapes are presented. The main evaluation point is located at y = 0, flanked by the additional evaluation points (all points located at x = 100 m).

Table B.1: 3DShape2_Straight results.

y	-50	-40	-30	-20	-10	0	10	20	30	40	50
Flat terrain											
$u_{z,RMS}$ [m]	1.32E-12	1.45E-12	1.59E-12	1.72E-12	1.82E-12	1.86E-12	1.82E-12	1.72E-12	1.59E-12	1.45E-12	1.32E-12
% of flat terrain	100%	100%	100%	100%	100%	100%	100%	100%	100%	100%	100%
[1]3DShape2[1_-1]_Straight											
$u_{z,RMS}$ [m]	1.11E-12	1.07E-12	1.12E-12	1.26E-12	1.39E-12	1.44E-12	1.39E-12	1.26E-12	1.12E-12	1.07E-12	1.11E-12
% of flat terrain	83.8 %	73.8 %	70.3 %	73.0 %	76.4 %	77.6 %	76.4 %	73.0 %	70.3 %	73.8 %	83.8 %
[-1]3DShape2[1_-1]_Straight											
$u_{z,RMS}$ [m]	9.81E-13	1.03E-12	1.15E-12	1.28E-12	1.36E-12	1.39E-12	1.36E-12	1.28E-12	1.15E-12	1.03E-12	9.81E-13
% of flat terrain	74.1 %	71.2 %	72.3 %	74.0 %	74.9 %	75.0 %	74.9 %	74.0 %	72.3 %	71.2 %	74.2 %
[1]3DShape2[1_1]_Straight											
$u_{z,RMS}$ [m]	9.81E-13	1.15E-12	1.40E-12	1.57E-12	1.65E-12	1.67E-12	1.65E-12	1.57E-12	1.40E-12	1.15E-12	9.81E-13
% of flat terrain	74.1 %	79.2 %	88.0 %	91.3 %	90.9 %	90.1 %	90.9 %	91.3 %	88.0 %	79.2 %	74.1 %
[-1]3DShape2[1_1]_Straight											
$u_{z,RMS}$ [m]	1.69E-12	1.72E-12	1.70E-12	1.66E-12	1.64E-12	1.63E-12	1.64E-12	1.67E-12	1.70E-12	1.72E-12	1.69E-12
% of flat terrain	127.7 %	118.6 %	107.2 %	96.6 %	90.1 %	87.9 %	90.1 %	96.6 %	107.2 %	118.7 %	127.7 %

Table B.2: 3DShape3_Straight results.

y	-50	-40	-30	-20	-10	0	10	20	30	40	50
Flat terrain											
$u_{z,RMS}$ **[m]**	1.32E-12	1.45E-12	1.59E-12	1.72E-12	1.82E-12	1.86E-12	1.82E-12	1.72E-12	1.59E-12	1.45E-12	1.32E-12
% of flat terrain	100%	100%	100%	100%	100%	100%	100%	100%	100%	100%	100%
[1]3DShape3[1_-1_1]_Straight											
$u_{z,RMS}$ **[m]**	1.08E-12	1.24E-12	1.34E-12	1.43E-12	1.51E-12	1.55E-12	1.51E-12	1.43E-12	1.34E-12	1.24E-12	1.08E-12
% of flat terrain	81.6 %	85.0 %	84.6 %	83.1 %	83.1 %	83.3 %	83.1 %	83.1 %	84.6 %	85.0 %	81.6 %
[-1]3DShape3[1_-1_1]_Straight											
$u_{z,RMS}$ **[m]**	1.07E-12	1.20E-12	1.33E-12	1.42E-12	1.47E-12	1.48E-12	1.47E-12	1.42E-12	1.33E-12	1.20E-12	1.07E-12
% of flat terrain	80.9 %	82.4 %	83.6 %	82.6 %	80.7 %	79.7 %	80.7 %	82.6 %	83.6 %	82.4 %	80.9 %
[1]3DShape3[1_1_1]_Straight											
$u_{z,RMS}$ **[m]**	1.16E-12	1.26E-12	1.44E-12	1.61E-12	1.71E-12	1.74E-12	1.71E-12	1.61E-12	1.44E-12	1.26E-12	1.16E-12
% of flat terrain	87.4 %	86.5 %	90.9 %	93.5 %	93.9 %	93.6 %	93.9 %	93.5 %	90.9 %	86.5 %	87.4 %
[-1]3DShape3[1_1_1]_Straight											
$u_{z,RMS}$ **[m]**	2.05E-12	2.31E-12	2.49E-12	2.57E-12	2.60E-12	2.60E-12	2.60E-12	2.57E-12	2.49E-12	2.31E-12	2.05E-12
% of flat terrain	155.2 %	159.4 %	156.5 %	149.1 %	142.7 %	140.1 %	142.7 %	149.1 %	156.5 %	159.4 %	155.2 %

Table B.3: 3DShape4_Straight results.

y	-50	-40	-30	-20	-10	0	10	20	30	40	50
Flat terrain											
$u_{z,RMS}$ **[m]**	1.32E-12	1.45E-12	1.59E-12	1.72E-12	1.82E-12	1.86E-12	1.82E-12	1.72E-12	1.59E-12	1.45E-12	1.32E-12
% of flat terrain	100%	100%	100%	100%	100%	100%	100%	100%	100%	100%	100%
[1]3DShape4[1_-1_1_-1]_Straight											
$u_{z,RMS}$ **[m]**	1.10E-12	1.22E-12	1.33E-12	1.45E-12	1.54E-12	1.58E-12	1.54E-12	1.45E-12	1.33E-12	1.22E-12	1.10E-12
% of flat terrain	83.3 %	84.1 %	83.8 %	83.9 %	84.6 %	84.8 %	84.6 %	83.9 %	83.8 %	84.0 %	83.3 %
[-1]3DShape4[1_-1_1_-1]_Straight											
$u_{z,RMS}$ **[m]**	1.00E-12	1.11E-12	1.23E-12	1.36E-12	1.46E-12	1.49E-12	1.45E-12	1.36E-12	1.23E-12	1.11E-12	1.00E-12
% of flat terrain	76.0 %	76.2 %	77.6 %	79.0 %	80.0 %	80.2 %	80.0 %	79.0 %	77.5 %	76.2 %	76.0 %
[1]3DShape4[1_1_1_1]_Straight											
$u_{z,RMS}$ **[m]**	1.18E-12	1.32E-12	1.49E-12	1.65E-12	1.76E-12	1.80E-12	1.76E-12	1.65E-12	1.49E-12	1.32E-12	1.18E-12
% of flat terrain	89.2 %	90.9 %	93.9 %	95.9 %	96.7 %	96.8 %	96.7 %	95.9 %	93.9 %	90.8 %	89.2 %
[-1]3DShape4[1_1_1_1]_Straight											
$u_{z,RMS}$ **[m]**	1.92E-12	2.21E-12	2.41E-12	2.52E-12	2.56E-12	2.57E-12	2.56E-12	2.52E-12	2.41E-12	2.21E-12	1.92E-12
% of flat terrain	144.8 %	151.8 %	151.9 %	146.4 %	140.8 %	138.4 %	140.8 %	146.4 %	151.9 %	151.8 %	144.8 %

Table B.4: 3DShape2_45 results.

y	-50	-40	-30	-20	-10	0	10	20	30	40	50
Flat terrain											
$u_{z,RMS}$ [m]	1.32E-12	1.45E-12	1.59E-12	1.72E-12	1.82E-12	1.86E-12	1.82E-12	1.72E-12	1.59E-12	1.45E-12	1.32E-12
% of flat terrain	100%	100%	100%	100%	100%	100%	100%	100%	100%	100%	100%
[1]3DShape2[1_-1]_45_RightEdge											
$u_{z,RMS}$ [m]	7.52E-13	7.75E-13	9.77E-13	1.32E-12	1.71E-12	2.00E-12	2.18E-12	2.49E-12	2.16E-12	1.09E-12	7.36E-13
% of flat terrain	56.9 %	53.4 %	61.4 %	76.7 %	93.9 %	107.9 %	119.7 %	144.8 %	135.8 %	74.9 %	55.7 %
[-1]3DShape2[1_-1]_45_RightEdge											
$u_{z,RMS}$ [m]	1.27E-12	1.04E-12	8.25E-13	7.83E-13	8.64E-13	9.43E-13	9.79E-13	8.98E-13	8.04E-13	8.14E-13	9.05E-13
% of flat terrain	96.1 %	71.7 %	51.9 %	45.4 %	47.5 %	50.8 %	53.8 %	52.1 %	50.6 %	56.0 %	68.4 %
[1]3DShape2[1_1]_45_RightEdge											
$u_{z,RMS}$ [m]	9.46E-13	1.25E-12	1.57E-12	1.60E-12	1.56E-12	1.57E-12	1.49E-12	1.49E-12	1.47E-12	1.22E-12	1.02E-12
% of flat terrain	71.5 %	85.9 %	98.9 %	93.0 %	85.8 %	84.3 %	81.9 %	86.5 %	92.4 %	83.7 %	77.3 %
[-1]3DShape2[1_1]_45_RightEdge											
$u_{z,RMS}$ [m]	1.60E-12	1.68E-12	1.71E-12	1.79E-12	1.88E-12	1.87E-12	1.78E-12	1.55E-12	1.30E-12	1.20E-12	1.28E-12
% of flat terrain	120.9 %	115.6 %	107.3 %	103.8 %	103.5 %	100.9 %	97.9 %	90.2 %	81.6 %	82.8 %	97.1 %
[1]3DShape2[1_-1]_45_Middle											
$u_{z,RMS}$ [m]	7.41E-13	7.21E-13	7.59E-13	8.99E-13	1.01E-12	1.05E-12	1.03E-12	8.95E-13	6.74E-13	5.39E-13	7.57E-13
% of flat terrain	56.0 %	49.6 %	47.8 %	52.2 %	55.5 %	56.8 %	56.4 %	51.9 %	42.4 %	37.1 %	57.2 %
[-1]3DShape2[1_-1]_45_Middle											
$u_{z,RMS}$ [m]	1.55E-12	1.85E-12	2.13E-12	2.33E-12	2.20E-12	1.63E-12	9.58E-13	7.06E-13	8.09E-13	1.04E-12	1.13E-12
% of flat terrain	116.8 %	127.4 %	133.8 %	135.0 %	120.8 %	88.0 %	52.7 %	41.0 %	50.9 %	71.8 %	85.2 %

Table B.5: 3DShape3_45 results.

y	-50	-40	-30	-20	-10	0	10	20	30	40	50
Flat terrain											
$u_{z,RMS}$ [m]	1.32E-12	1.45E-12	1.59E-12	1.72E-12	1.82E-12	1.86E-12	1.82E-12	1.72E-12	1.59E-12	1.45E-12	1.32E-12
% of flat terrain	100%	100%	100%	100%	100%	100%	100%	100%	100%	100%	100%
[1]3DShape3[1_-1_1]_45_RightEdge											
$u_{z,RMS}$ [m]	1.25E-12	1.40E-12	1.40E-12	1.34E-12	1.34E-12	1.38E-12	1.45E-12	1.50E-12	1.56E-12	1.59E-12	1.31E-12
% of flat terrain	94.3 %	96.7 %	87.9 %	77.5 %	73.7 %	74.4 %	79.9 %	87.0 %	98.3 %	109.5 %	99.3 %
[-1]3DShape3[1_-1_1]_45_RightEdge											
$u_{z,RMS}$ [m]	8.80E-13	1.10E-12	1.27E-12	1.35E-12	1.45E-12	1.49E-12	1.32E-12	1.11E-12	1.15E-12	1.09E-12	9.18E-13
% of flat terrain	66.6 %	75.9 %	79.6 %	78.6 %	79.9 %	80.3 %	72.5 %	64.6 %	72.6 %	74.9 %	69.4 %
[1]3DShape3[1_1_1]_45_RightEdge											
$u_{z,RMS}$ [m]	1.14E-12	1.33E-12	1.58E-12	1.61E-12	1.66E-12	1.84E-12	1.92E-12	1.71E-12	1.35E-12	1.09E-12	1.09E-12
% of flat terrain	85.9 %	91.8 %	99.2 %	93.3 %	91.0 %	99.1 %	105.3 %	99.5 %	85.1 %	75.3 %	82.2 %
[-1]3DShape3[1_1_1]_45_RightEdge											
$u_{z,RMS}$ [m]	2.01E-12	2.06E-12	2.12E-12	2.27E-12	2.36E-12	2.22E-12	2.02E-12	2.06E-12	2.29E-12	2.37E-12	2.11E-12
% of flat terrain	151.9 %	142.2 %	133.6 %	131.9 %	129.6 %	119.8 %	111.2 %	119.7 %	144.3 %	163.5 %	159.2 %
[1]3DShape3[1_-1_1]_45_Middle											
$u_{z,RMS}$ [m]	8.54E-13	1.06E-12	1.22E-12	1.32E-12	1.34E-12	1.30E-12	1.28E-12	1.19E-12	1.12E-12	1.01E-12	8.06E-13
% of flat terrain	64.5 %	72.6 %	76.9 %	76.6 %	73.6 %	70.1 %	70.1 %	68.8 %	70.6 %	69.7 %	61.0 %
[-1]3DShape3[1_-1_1]_45_Middle											
$u_{z,RMS}$ [m]	1.19E-12	1.18E-12	1.22E-12	1.34E-12	1.51E-12	1.68E-12	1.78E-12	1.63E-12	1.22E-12	1.05E-12	1.03E-12
% of flat terrain	90.2 %	81.1 %	76.5 %	77.7 %	82.9 %	90.4 %	98.0 %	94.8 %	76.9 %	72.6 %	77.9 %

Table B.6: 3DShape4_45 results.

y	-50	-40	-30	-20	-10	0	10	20	30	40	50
Flat terrain											
$u_{z,RMS}$ [m]	1.32E-12	1.45E-12	1.59E-12	1.72E-12	1.82E-12	1.86E-12	1.82E-12	1.72E-12	1.59E-12	1.45E-12	1.32E-12
% of flat terrain	100%	100%	100%	100%	100%	100%	100%	100%	100%	100%	100%
[1]3DShape4[1_-1_1_-1]_45_RightEdge											
$u_{z,RMS}$ [m]	9.03E-13	1.12E-12	1.44E-12	1.75E-12	1.90E-12	1.75E-12	1.50E-12	1.32E-12	1.13E-12	1.02E-12	8.71E-13
% of flat terrain	68.3 %	77.4 %	90.8 %	101.7 %	104.5 %	94.1 %	82.6 %	76.5 %	71.4 %	70.2 %	65.9 %
[-1]3DShape4[1_-1_1_-1]_45_RightEdge											
$u_{z,RMS}$ [m]	1.23E-12	1.18E-12	1.20E-12	1.29E-12	1.34E-12	1.33E-12	1.32E-12	1.27E-12	1.08E-12	1.03E-12	1.04E-12
% of flat terrain	93.0 %	81.0 %	75.3 %	75.1 %	73.9 %	71.6 %	72.6 %	73.5 %	68.1 %	71.0 %	78.4 %
[1]3DShape4[1_1_1_1]_45_RightEdge											
$u_{z,RMS}$ [m]	1.15E-12	1.38E-12	1.63E-12	1.73E-12	1.80E-12	1.89E-12	1.89E-12	1.82E-12	1.61E-12	1.43E-12	1.26E-12
% of flat terrain	87.3 %	95.0 %	102.7 %	100.5 %	99.1 %	102.0 %	103.9 %	105.5 %	101.4 %	98.8 %	95.6 %
[-1]3DShape4[1_1_1_1]_45_RightEdge											
$u_{z,RMS}$ [m]	1.91E-12	2.15E-12	2.29E-12	2.41E-12	2.45E-12	2.43E-12	2.48E-12	2.48E-12	2.40E-12	2.29E-12	2.03E-12
% of flat terrain	144.3 %	148.3 %	143.9 %	140.0 %	134.8 %	131.0 %	136.2 %	144.2 %	151.2 %	158.0 %	153.7 %
[1]3DShape4[1_-1_1_-1]_45_Middle											
$u_{z,RMS}$ [m]	8.57E-13	9.47E-13	1.15E-12	1.30E-12	1.46E-12	1.59E-12	1.52E-12	1.29E-12	1.13E-12	9.22E-13	7.85E-13
% of flat terrain	64.8 %	65.2 %	72.2 %	75.6 %	80.1 %	85.9 %	83.5 %	74.7 %	71.0 %	63.5 %	59.3 %
[-1]3DShape4[1_-1_1_-1]_45_Middle											
$u_{z,RMS}$ [m]	1.33E-12	1.61E-12	1.70E-12	1.61E-12	1.49E-12	1.37E-12	1.30E-12	1.26E-12	1.11E-12	8.81E-13	8.15E-13
% of flat terrain	100.3 %	111.0 %	107.0 %	93.4 %	81.7 %	73.8 %	71.7 %	73.2 %	69.9 %	60.6 %	61.6 %

Table B.7: 3DShape2_Check results.

y	-50	-40	-30	-20	-10	0	10	20	30	40	50
Flat terrain											
$u_{z,RMS}$ [m]	1.32E-12	1.45E-12	1.59E-12	1.72E-12	1.82E-12	1.86E-12	1.82E-12	1.72E-12	1.59E-12	1.45E-12	1.32E-12
% of flat terrain	100%	100%	100%	100%	100%	100%	100%	100%	100%	100%	100%
[1]3DShape2[1_-1]_Check_RightEdge											
$u_{z,RMS}$ [m]	6.86E-13	6.78E-13	9.59E-13	1.20E-12	1.27E-12	1.38E-12	1.41E-12	1.39E-12	1.08E-12	6.34E-13	7.79E-13
% of flat terrain	51.8 %	46.7 %	60.4 %	69.7 %	69.7 %	74.6 %	77.6 %	80.5 %	68.0 %	43.7 %	58.9 %
[1]3DShape2[1_1]_Check_RightEdge											
$u_{z,RMS}$ [m]	8.70E-13	1.17E-12	1.52E-12	1.50E-12	1.11E-12	9.44E-13	1.11E-12	1.50E-12	1.52E-12	1.17E-12	8.70E-13
% of flat terrain	65.8 %	80.2 %	95.9 %	87.3 %	61.1 %	50.9 %	61.1 %	87.3 %	95.9 %	80.3 %	65.8 %
[-1]3DShape2[1_1]_Check_RightEdge											
$u_{z,RMS}$ [m]	1.89E-12	1.77E-12	1.66E-12	1.98E-12	2.75E-12	3.22E-12	2.76E-12	1.98E-12	1.66E-12	1.77E-12	1.89E-12
% of flat terrain	142.8 %	122.0 %	104.6 %	115.0 %	151.4 %	173.4 %	151.4 %	115.0 %	104.7 %	122.0 %	142.8 %
[1]3DShape2[1_-1]_Check_Middle											
$u_{z,RMS}$ [m]	1.02E-12	1.54E-12	1.50E-12	1.33E-12	1.69E-12	1.94E-12	1.69E-12	1.33E-12	1.50E-12	1.54E-12	1.02E-12
% of flat terrain	77.1 %	106.2 %	94.1 %	77.3 %	92.8 %	104.6 %	92.8 %	77.3 %	94.1 %	106.2 %	77.2 %
[-1]3DShape2[1_-1]_Check_Middle											
$u_{z,RMS}$ [m]	1.53E-12	1.71E-12	1.43E-12	1.15E-12	1.60E-12	2.10E-12	1.60E-12	1.15E-12	1.43E-12	1.71E-12	1.53E-12
% of flat terrain	115.7 %	117.5 %	90.3 %	66.8 %	88.2 %	113.3 %	88.2 %	66.8 %	90.3 %	117.5 %	115.8 %

Table B.8: 3DShape3_Check results.

y	-50	-40	-30	-20	-10	0	10	20	30	40	50
Flat terrain											
$u_{z,RMS}$ [m]	1.32E-12	1.45E-12	1.59E-12	1.72E-12	1.82E-12	1.86E-12	1.82E-12	1.72E-12	1.59E-12	1.45E-12	1.32E-12
% of flat terrain	100%	100%	100%	100%	100%	100%	100%	100%	100%	100%	100%
[1]3DShape3[1_-1_1]_Check_RightEdge											
$u_{z,RMS}$ [m]	9.50E-13	1.21E-12	1.44E-12	1.50E-12	1.59E-12	1.45E-12	1.20E-12	1.16E-12	9.23E-13	7.53E-13	8.11E-13
% of flat terrain	71.8 %	83.3 %	90.7 %	86.8 %	87.3 %	78.2 %	66.0 %	67.4 %	58.1 %	51.8 %	61.3 %
[1]3DShape3[1_1_1]_Check_RightEdge											
$u_{z,RMS}$ [m]	1.24E-12	1.35E-12	1.49E-12	1.77E-12	1.90E-12	1.96E-12	1.90E-12	1.77E-12	1.49E-12	1.35E-12	1.24E-12
% of flat terrain	93.8 %	92.9 %	93.5 %	102.9 %	104.3 %	105.6 %	104.3 %	103.0 %	93.5 %	92.9 %	93.8 %
[-1]3DShape3[1_1_1]_Check_RightEdge											
$u_{z,RMS}$ [m]	1.84E-12	2.05E-12	2.35E-12	2.52E-12	2.58E-12	2.66E-12	2.58E-12	2.52E-12	2.35E-12	2.05E-12	1.84E-12
% of flat terrain	139.2 %	141.0 %	147.9 %	146.4 %	141.7 %	143.4 %	141.7 %	146.4 %	147.9 %	141.0 %	139.2 %
[1]3DShape3[1_-1_1]_Check_Middle											
$u_{z,RMS}$ [m]	7.43E-13	7.79E-13	1.08E-12	1.42E-12	1.67E-12	1.91E-12	1.67E-12	1.42E-12	1.08E-12	7.79E-13	7.44E-13
% of flat terrain	56.2 %	53.6 %	67.8 %	82.4 %	91.8 %	103.0 %	91.8 %	82.4 %	67.8 %	53.6 %	56.2 %
[-1]3DShape3[1_-1_1]_Check_Middle											
$u_{z,RMS}$ [m]	1.38E-12	1.24E-12	1.17E-12	1.14E-12	1.27E-12	1.45E-12	1.27E-12	1.14E-12	1.17E-12	1.24E-12	1.38E-12
% of flat terrain	104.6 %	85.2 %	73.5 %	66.0 %	69.6 %	78.2 %	69.6 %	66.0 %	73.5 %	85.2 %	104.6 %

Table B.9: 3DShape4_Check results.

y	-50	-40	-30	-20	-10	0	10	20	30	40	50
Flat terrain											
$u_{z,RMS}$ [m]	1.32E-12	1.45E-12	1.59E-12	1.72E-12	1.82E-12	1.86E-12	1.82E-12	1.72E-12	1.59E-12	1.45E-12	1.32E-12
% of flat terrain	100%	100%	100%	100%	100%	100%	100%	100%	100%	100%	100%
[1]3DShape4[1_-1_1_-1}_Check_RightEdge											
$u_{z,RMS}$ [m]	1.19E-12	1.36E-12	1.36E-12	1.39E-12	1.25E-12	1.31E-12	1.43E-12	1.39E-12	1.19E-12	1.10E-12	1.12E-12
% of flat terrain	89.8 %	93.9 %	85.6 %	80.5 %	68.9 %	70.8 %	78.4 %	81.0 %	74.6 %	75.7 %	84.8 %
[1]3DShape4[1_1_1_1}_Check_RightEdge											
$u_{z,RMS}$ [m]	1.28E-12	1.43E-12	1.67E-12	1.83E-12	1.92E-12	1.99E-12	1.92E-12	1.83E-12	1.67E-12	1.43E-12	1.28E-12
% of flat terrain	96.6 %	98.6 %	105.2 %	106.1 %	105.8 %	107.3 %	105.8 %	106.1 %	105.1 %	98.6 %	96.5 %
[-1]3DShape4[1_1_1_1}_Check_RightEdge											
$u_{z,RMS}$ [m]	1.69E-12	1.99E-12	2.21E-12	2.36E-12	2.38E-12	2.38E-12	2.38E-12	2.36E-12	2.21E-12	1.99E-12	1.69E-12
% of flat terrain	127.7 %	136.7 %	139.1 %	136.9 %	130.7 %	128.1 %	130.7 %	137.0 %	139.1 %	136.7 %	127.7 %
[1]3DShape4[1_-1_1_-1}_Check_Middle											
$u_{z,RMS}$ [m]	1.11E-12	1.19E-12	1.37E-12	1.46E-12	1.42E-12	1.50E-12	1.42E-12	1.46E-12	1.37E-12	1.19E-12	1.11E-12
% of flat terrain	84.3 %	81.9 %	85.9 %	84.6 %	78.0 %	80.8 %	78.0 %	84.6 %	85.9 %	81.9 %	84.3 %
[-1]3DShape4[1_-1_1_-1}_Check_Middle											
$u_{z,RMS}$ [m]	1.19E-12	1.21E-12	1.18E-12	1.12E-12	1.24E-12	1.49E-12	1.24E-12	1.12E-12	1.18E-12	1.21E-12	1.19E-12
% of flat terrain	90.2 %	83.1 %	74.2 %	64.7 %	68.0 %	80.1 %	68.0 %	64.7 %	74.2 %	83.1 %	90.2 %